Hygromechanical mechanisms of wood cell wall revealed by molecular modeling and mixture rule analysis

Chi Zhang, Mingyang Chen, Sinan Keten, Benoit Coasne, Dominique Derome, Jan Carmeliet

MATERIALS SCIENCE

Hygromechanical mechanisms of wood cell wall revealed by molecular modeling and mixture rule analysis

Chi Zhang[1]*, Mingyang Chen[1], Sinan Keten[2], Benoit Coasne[3], Dominique Derome[4], Jan Carmeliet[1]

Despite the thousands of years of wood utilization, the mechanisms of wood hygromechanics remain barely elucidated, owing to the nanoscopic system size and highly coupled physics. This study uses molecular dynamics simulations to systematically characterize wood polymers, their mixtures, interface, and composites, yielding an unprecedented micromechanical dataset including swelling, mechanical weakening, and hydrogen bonding, over the full hydration range. The rich data reveal the mechanism of wood cell wall hygromechanics: Cellulose fiber dominates the mechanics of cell wall along the longitudinal direction. Hemicellulose glues lignin and cellulose fiber together defining the cell wall mechanics along the transverse direction, and water severely disturbs the hemicellulose-related hydrogen bonds. In contrast, lignin is rather hydration independent and serves mainly as a space filler. The moisture-induced highly anisotropic swelling and weakening of wood cell wall is governed by the interplay of cellulose reinforcement, mechanical degradation of matrix, and fiber-matrix interface.

INTRODUCTION

Wood is presumably the most abundant biomaterial on Earth showing a combination of specific properties like high stiffness and strength in combination with low density and low thermal conductivity. For thousands of years, it has been used as fuel, tools, building materials, and so on, covering vital aspects of human lives. By means of modern nanotechnologies, the utility of wood can be extended far beyond: Wood provides sustainable and environment-friendly solutions to future advanced systems, for example, green electronic devices with ion regulation capability and even transparency (*1*). The exploitation of the full potential of wood calls for a thorough understanding of its mechanics and hierarchical structure, especially on the nanoscale.

The mechanics of wood stems from the thick cell walls, particularly the S2 layer, which takes up ~80% of the total thickness (*2*). Of note, this study focuses on softwood for its substantial economic value and prevalence in the northern hemisphere, including northern Europe, North America, and Russia (*3*). Fundamentally, the S2 layer is a fiber-reinforced composite where the cellulose crystals of a diameter of ~3 nm are embedded in a compliant matrix of hemicellulose and lignin (LGN) with a thickness of 3 to 14 nm (*4*). The crystalline cellulose (CC) fibers, which feature densely packed chains saturated with hydrogen bonds (HBs), display a tensile stiffness up to ~160 GPa along the axial direction, comparable to Kevlar. The exact material configuration of cell wall is still under debate because the nanoscopic interactions are beyond the detection limits of contemporary experimental techniques. Spectroscopy methods, e.g., multidimensional solid-state nuclear magnetic resonance, can detect the material arrangement and interactions of matrix components (*5*, *6*), while consensus has yet to be achieved. Moreover, the mechanical influence of ubiquitous interactions between the cell wall components remains concealed. Although wood researchers often attribute the excellent wood mechanics to the so-called "nanoeffects," real nanoscale evidence is still lacking (*7*). Powerful tools are urgently needed to tackle this challenge.

In addition to the ultrafine size of the cell wall structure, the mechanical behaviors of wood are formidably convoluted. Wood is highly hygroscopic, and water sorption induces profound physical and mechanical alterations, such as anisotropic swelling, mechanical weakening, and shape memory effect. These behaviors involve intricate molecular interactions and the influencing factors, such as hydration, porosity, hydrogen bonding, and material interface, are strongly coupled, impeding the efforts of explication and leaving the microscopic mechanisms barely elucidated (*8*–*10*).

To circumvent the experimental difficulties, computational studies, especially finite element models with micromechanics (*11*) and poromechanics (*12*), are proposed. These models are designed to reproduce macroscopic behaviors, such as the mechanosorptive effect and the influence of microfibril angle on cell wall modulus, whereas they rarely probe nanoscopic mechanisms. In addition, the models require material properties as input parameters. However, the properties used in almost all the models are more or less the same because there is only a limited number of available experimental sources, as listed in table S2. Even the available data should be used with caution. For example, the widely acknowledged hygromechanical data from Cousins (*13*, *14*) are measured from powder samples that are chemically different from native wood. A consistent set of hygromechanical data for wood polymers, as well as for their interfaces, is highly desirable.

Few studies use molecular simulations to explore the nanoscopic structure-property-function relationships of the plant cell wall (*15*–*19*). Kulasinski *et al.* (*20*) proposed an advanced molecular model of S2 layer surrogate system, consisting of CC microfibrils embedded in galactoglucomannan (GGM) and surrounded by LGN of low polymerization degree. Nevertheless, the existing modeling works

[1]Chair of Building Physics, Department of Mechanical and Process Engineering, ETH Zurich, 8092 Zurich, Switzerland. [2]Department of Civil and Environmental Engineering, Northwestern University, Evanston, IL 60208-3109, USA. [3]Université Grenoble Alpes, CNRS, LIPhy, 38000 Grenoble, France. [4]Department of Civil and Building Engineering, Université de Sherbrooke, Sherbrooke, QC J1K 2R1, Canada. *Corresponding author. Email: outlook.zhangchi@gmail.com

deviate from reality over several fundamental aspects, such as the absence of hydration effect and material composition and arrangement. Particularly missing is a cell wall atomistic model that complies with the most advanced knowledge of wood science. The only way to thoroughly understand the molecular interactions between biopolymer components is via comprehensive investigation of components individually and their composites collectively. This will clarify the individual role of various components of wood, thus providing guidance to the improvement of the performance of wood-derived materials, e.g., chemically modified wood and derived cellulose scaffold that attracted tremendous attention in recent years.

In this study, we use molecular dynamics (MD) simulations to understand the structural, physical, and mechanical impact of hydration on wood cell wall. Polymer components, their composites and interfaces, and a state-of-the-art S2 cell wall layer model are proposed and characterized systematically. The yielded unprecedented micromechanical dataset enables comprehensive rule of mixture (RoM) analyses, revealing the working mechanism of cell wall that is otherwise unobtainable. It is demonstrated that the interphases exhibit densities or mechanical properties distinct from bulk material. Although the matrix itself is soft and isotropic in bulk, its interphase is stiff and anisotropic owing to the influence of cellulose fiber. Hydration induces the weakening of wood cell wall by causing mechanical degradation of matrix and fiber-matrix interface while leaving the CC fiber mostly intact. Cellulose fiber defines the strong orthotropy of cell wall, as indicated by the mechanical stiffness, swelling strain, etc. Hemicellulose glues LGN and cellulose fiber together, and water severely disturbs the hemicellulose-related HBs. In contrast, LGN is rather hydration independent and serves mainly as a space filler. These findings extend the current understanding of wood cell wall down to the molecular scale and elucidate the physics of moisture-related mechanical phenomena. The proposed numerical methodology and the representative molecular models open up research opportunities, e.g., water-logged archeological wood preservation (*21*).

RESULTS

Hygromechanics of S2-related materials and composites

This section presents the hygromechanical characterization, including hygroscopic swelling and moisture-induced mechanical weakening of S2-related materials and composites, namely, components arabinoglucuronoxylan (AGX), GGM, uncondensed lignin (uLGN), condensed lignin (cLGN), mixtures M1 and M2, and composite S2.

Hygroscopic swelling

The hygroscopic swelling is characterized as the uniaxial swelling strain as a function of moisture content, as shown in Fig. 1. In wood polymers, such swelling is generally linear with moisture content except for some initial nonlinearity explained by an initial porosity filling mechanism (*20*). The studied material systems are of nanometer sizes and show nanoscale porosity. Water molecules first enter the existing pore space, explaining the lower swelling at low moisture content. At higher moisture content, new pore space between the polymeric chains is created and filled by water molecules, resulting in a linear swelling versus moisture content. Therefore, the swelling strain will be a piecewise function of moisture content as shown in Eq. 1.

For the studied systems, at $m \sim 0.3$, the uniaxial swelling strain is around 0.1, agreeing well with experimental reports on wood cell wall of Douglas fir (*22*). More recent x-ray tomographic study of spruce cell wall micropillar reported the average of uniaxial swelling of ~0.08 at a relative humidity (RH) ~ 85% (*23*), which is considerably larger than that of spruce at macroscale, i.e., ~0.04 at RH ~ 90%, because the free swelling at cellular wall level is hindered by the other cell wall layers, namely, S1 and S3 and, at higher scales, by the presence of rays and growth rings (*23*).

To model the swelling curves, a piecewise linear function is proposed

$$\varepsilon = \begin{cases} \beta_A m, & | m < m_A \\ \beta_A m_A + \beta_B (m - m_A), & | m \geq m_A \end{cases} \quad (1)$$

The swelling coefficient is β_A for $m < m_A$ and is β_B for $m \geq m_A$. The incremental form of Eq. 1 is

$$\Delta\varepsilon = \begin{cases} \beta_A \Delta m, & | m < m_A \\ \beta_B \Delta m, & | m \geq m_A \end{cases} \quad (2)$$

Following these forms, the swelling curves are shown as lines in Fig. 1. The parameters are summarized in Table 1.

The swelling in the moisture range between dry and m_A is characterized by a different initial regime. For all material systems, the swelling coefficient β_A is lower than β_B. The initial porosity needs to be filled first, and therefore, the swelling is less pronounced at a lower moisture level.

The swelling coefficient β_B describes the swelling in the higher moisture content range. It is interesting to find that M1, which consists of AGX and uLGN, shows slightly higher swelling than its components. This indicates the effect of blending, which will be scrutinized in a later section using mixture rule analyses. In contrast, the blending of GGM and cLGN does not hint at abnormality, and swelling strain of M1 is between its components.

The swelling of S2 is transversely isotropic and thus described by longitudinal and transverse swelling coefficients. The transverse swelling is ~170 times the longitudinal swelling, which clearly supports that the anisotropic swelling of wood originates from cell wall material level (*23*). This anisotropy is caused by the reinforcing effect of the stiff fibers that do not adsorb water and do not swell (*24*). The transverse swelling of S2 is comparable to that of mixtures M1 and M2. Of note, there is a caveat for the interpretation of the swelling of S2. The moisture content of S2 is defined as the ratio of the mass of water to dry matrix, which takes ~56% of the dry mass of full S2. The mass of CC is excluded for the sake of comparability with mixtures M1 and M2.

The volumetric swelling can be calculated from uniaxial swelling using

$$\varepsilon_V = (1 + \varepsilon_x)(1 + \varepsilon_y)(1 + \varepsilon_z) - 1 \quad (3)$$

For isotropic material, $\varepsilon_x = \varepsilon_y = \varepsilon_z = \varepsilon$. For transversely isotropic material, $\varepsilon_x = \varepsilon_y = \varepsilon_T$ and $\varepsilon_z = \varepsilon_L$. In the studied polymer systems, swelling is the result of the creation of new pore space. The porosity φ can therefore be determined directly from the volumetric swelling strain

$$\varphi = \frac{\varepsilon_V}{1 + \varepsilon_V} \quad (4)$$

The porosity will be used in the next sections to model the moisture dependence of elastic properties.

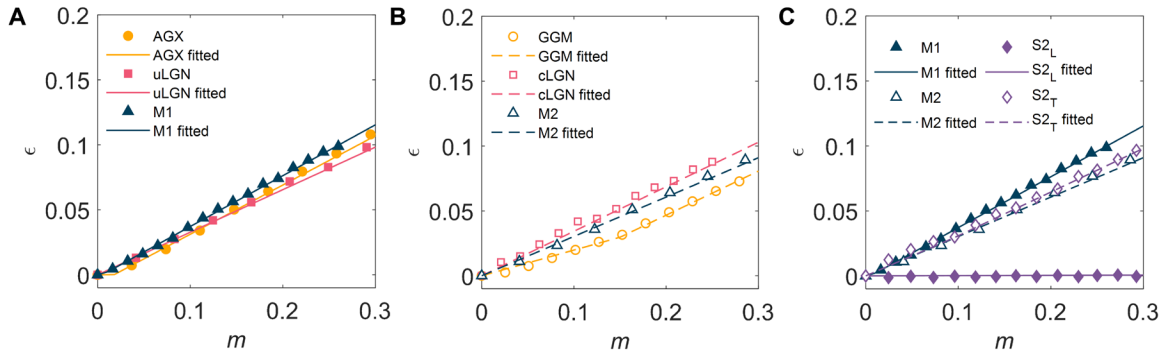

Fig. 1. Uniaxial hygroscopic swelling strain (ε) of the polymer systems as a function of moisture content (*m*). The MD measurements are represented by symbols and the fit by lines. (**A**) AGX, uLGN, and M1. (**B**) GGM, cLGN, and M2. (**C**) M1, M2, and S2.

Table 1. Parameters of uniaxial swelling strain and elastic moduli as a function of moisture content.

Material	β_A	m_A	β_B	K_0 (GPa)	A_K	E_0 (GPa)	A_E	G_0 (GPa)	A_G
AGX	0.010	0.018	0.379	5.658	1.660	4.418	2.818	2.122	3.598
GGM	0.198	0.150	0.340	4.653	0.420	4.957	3.497	2.176	4.291
uLGN	–	0	0.328	2.546	0.423	1.896	3.475	1.079	3.217
cLGN	–	0	0.343	2.734	0.067	1.875	1.791	0.791	1.789
M1	0.214	0.011	0.391	3.561	1.772	2.747	3.709	1.162	2.541
M2	–	0	0.303	4.182	1.007	3.470	4.071	1.665	3.818
S2L	–	0	0.002	–	–	43.764	0.931	2.038	5.164
S2T	0.308	0.096	0.336	–	–	3.540	5.242	0.624	4.753

Moisture-induced weakening

The schematics of mechanical tests are shown in Fig. 2A. Elastic moduli, namely, bulk, Young's, and shear moduli, are determined from the stress-strain curves of volumetric tension, uniaxial tension, and shear loading tests, respectively. All systems display a weakening trend upon hydration, as shown in Fig. 2 (B to K). Generally, hemicelluloses show higher mechanical stiffness than LGNs. The stiffness of the mixture, either M1 or M2, locates roughly in between that of their hemicellulose and LGN components.

The MD-measured moduli are in accordance with the available experimental data, most of which are Young's modulus. The Young's moduli of xylan and glucomannan range from 1.8 to 5.4 GPa (*25*–*27*) and 2.5 to 4.3 GPa (*25*), respectively. Reports on LGN Young's modulus give a range of 2.8 to 6.7 GPa (*13*, *28*, *29*), which is higher than the MD results here. This is possibly due to their specimen preparation, where LGN powder is molded into rods in which a pressure treatment densifies and stiffens the material. More experimental or simulation reports of wood-related polymers are included in table S2.

The S2 composite exhibits a longitudinal Young's modulus of 36 to 44 GPa, depending on the moisture content. Recent nanoindentation measurement suggested a similar range of 26 to 40 GPa (*30*). Yu *et al.* (*31*) showed that, as the moisture content is increased from 4.5 to 13.1%, the longitudinal modulus of Masson pine cell wall decreases nearly linearly from 20.4 to 16.9 GPa. Their values are lower than that of our model, which could be attributed to their lower loading rate, microfibril angle, different chemical composition, etc.

The longitudinal Young's modulus of S2 composite is ~10 times higher than the transverse one (*32*), which is due to the strong reinforcement effect by CC fiber. The axial Young's modulus of the CC fibrils is determined in MD by removing the matrix materials and then applying the protocol identical to the determination of the modulus of S2. It yields a value of 90 GPa, which is lower than the range, i.e., 100 to 160 GPa, determined in mechanical characterizations of crystalline fibril (*33*–*38*). The cellulose fibril in this study is weaker because the crystal here is not perfectly crystalline. More specifically, the chains at the surface of CC fibril moderately deviate from perfect crystal configurations as a consequence of relaxation and interaction with matrices, making the CC fibril weaker.

For homogeneous and isotropic materials, the bulk (K), Young's (E), and shear (G) moduli and Poisson's ratio (ν) follow the relations

$$G = \frac{3KE}{9K - E} \text{ and } \nu = \frac{3K - E}{6K} \quad (5)$$

It is confirmed by comparing all MD results that the material systems, namely, AGX, GGM, uLGN, cLGN, M1, and M2, comply with this relation. In other words, the shear moduli and Poisson's ratio can be well predicted using Eq. 5.

For transversely isotropic materials, Eq. 6 holds

$$G_{TT} = \frac{E_T}{2(1 + \nu_{TT})} \quad (6)$$

The S2 composite is found to comply roughly with this equation, as shown in Fig. 2K.

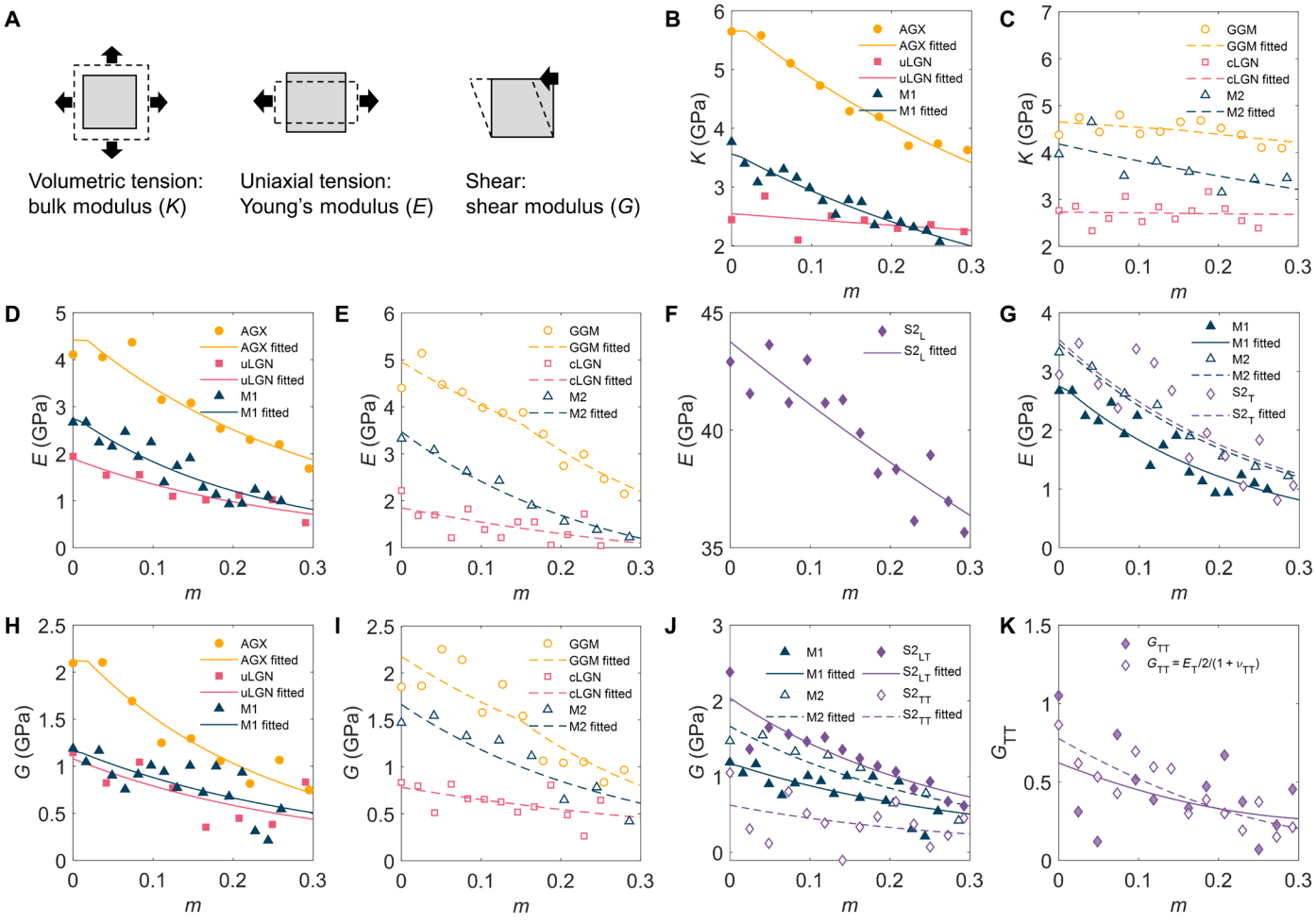

Fig. 2. Mechanical moduli as a function of moisture content. (**A**) Schematics of mechanical measurement. (**B** and **C**) Bulk moduli, where MD measurements are represented by symbols and fitted with Eq. 7 represented by lines, similarly hereinafter. (**D** to **G**) Young's moduli. (**H** to **J**) Shear moduli. (**K**) Consistency check of transverse shear moduli between MD measurement and prediction.

MD results show that the elastic properties depend on moisture content. In this work, such moisture dependence is modeled by porosity, as often done in literature (*39*), a quantity related to swelling strain as defined in Eq. 4. The following power laws are used

$$K = K_0(1-\varphi)^{A_K}, E = E_0(1-\varphi)^{A_E}, G = G_0(1-\varphi)^{A_G} \quad (7)$$

where K_0, E_0, and G_0 are the elastic properties at zero moisture content and A_K, A_E, and A_G are the power exponents. The fitted lines are shown in Fig. 2. The values of the parameters are listed in Table 1.

The exponents A_E, A_G, and A_K indicate the decay rate of moduli with increasing hydration. The hemicelluloses are found to show a more severe weakening compared to the LGNs. The transverse Young's modulus of S2 is also strongly influenced by hydration. In contrast, the longitudinal Young's modulus of S2 is the least weakened because of the strong reinforcement by the cellulose fibrils whose mechanical properties are independent of moisture content.

Mixture rule analyses

The compilation of hygromechanical data of wood polymers paves the way for comprehensive RoM analyses of density, swelling strain, and mechanical moduli. The results reveal the presence of interphases, i.e., the interaction between the different components, which are otherwise difficult to access through experiments.

Density

In practice, the density of wood is seen as an important indicator of wood mechanical performance (*40*). The densities of S2-related systems are measured in MD and listed in Table 2.

With the data of individual components, the density of the composites can be predicted by the fraction and density of the components. More specifically, with the knowledge of the volume fraction of component f_{vj}^0, weight coefficient w_j^0, and density ρ_j, of component j, the compound density ρ'_M can be predicted by the following RoM

$$\rho'_M = \sum_j f_{vj}^0 \rho_j \quad (8)$$

The prime symbol denotes prediction instead of MD measurement. The subscript M denotes the compound, i.e., M1, M2, or S2. The superscript 0 denotes the case where no interphase is present, showing the values before mixing. The volume fraction of component j is determined by the weight coefficient w_j^0 and density ρ_j of component j using the following equation

Table 2. Densities and volume fractions.

Material	ρ (g cm^{-3})	f^0_{vj}	
AGX	1.30	0.361	M1
uLGN	1.22	0.639	
GGM	1.24	0.615	M2
cLGN	1.30	0.385	
M1	1.28	0.242	S2
M2	1.24	0.360	
CC	1.50	0.398	
S2	1.28	–	

$$f^0_{vj} = \frac{w^0_j/\rho_j}{\sum_j w^0_j/\rho_j} \tag{9}$$

where $\frac{1}{(\sum_j w^0_j/\rho_j)}$ is the density of the compound system. The volume fractions according to Eq. 9 are summarized in Table 2.

As shown in Fig. 3A, the RoM prediction without interphase is always higher than the MD measurement. This difference stems from the fact that the simple mixing, as indicated by Eq. 8, assumes no interaction between components. However, in polymer blends, interactions between the components may strongly influence the overall composite performance (*41*). Therefore, the mixing rules should include an additional interaction term.

Here, the interaction region is referred to as the interphase, and an interphase component term denoted by subscript *I* is added to Eq. 8

$$\rho'_M = \sum_j f_{vj}\rho_j + f_{vI}\rho_I \tag{10}$$

Here, the volume fraction of the interphase f_{vI} is taken as the relative fraction of the number of HBs formed between the different components $\hat{\delta}$

$$f_{vi} = \hat{\delta} = \frac{\sum_{j\neq k} \#\mathrm{HB}_{jk}}{\sum_j \sum_k \#\mathrm{HB}_{jk} + \sum_j \#\mathrm{HB}_{jj}} \tag{11}$$

where $\#\mathrm{HB}_{jk} = \#\mathrm{HB}_{kj}$ denotes the number of HBs formed between components *j* and *k*, while $\#\mathrm{HB}_{jj}$ are the HBs within the component *j* itself. It is noted that, for the sake of simplicity, here, the number of HBs refers to the dry condition, as under moist condition the presence of water-related HBs complicate the determination of $\hat{\delta}$. The $\hat{\delta}$ for M1, M2, and S2 at dry state equal $\hat{\delta} = 0.210$, $\hat{\delta} = 0.176$, and $\hat{\delta} = 0.156$, respectively, as listed in Table 3.

The volume fractions of the other components are $(1 - \hat{\delta})$ times the value when no interphase is present

$$f_{vj} = (1 - \hat{\delta}) f^0_{vj} \tag{12}$$

For M1 and M2, the interphase densities are lower than the densities of the compound, as shown by the red bars in Fig. 3A, which may be the result of immiscibility. This implies that the components are interacting weakly or even slightly repulsively. The interphase density of S2 is significantly lower than that of the composite. In addition to the immiscibility, another reason might be the structural mismatch at the fiber-matrix interface.

In the following sections, the mixture rule analyses of M1 and M2 are first presented, and then comes the S2. They have to be separated in different sections, because M1 and M2 are isotropic, whereas S2 is transversely isotropic, and therefore, they do not follow the same equations of mixture rule.

Mixture rule analyses of matrices M1 and M2

The mixtures M1 and M2 are considered homogeneous and isotropic materials. The RoMs can predict their elastic moduli. Without an interphase, the RoMs read

$$\begin{aligned} K'_M &= f^0_{v1}K_1 + f^0_{v2}K_2 \\ E'_M &= f^0_{v1}E_1 + f^0_{v2}E_2 \\ G'_M &= f^0_{v1}G_1 + f^0_{v2}G_2 \\ f^0_{v1} + f^0_{v2} &= 1 \end{aligned} \tag{13}$$

When an interphase is present, the RoMs read

$$\begin{aligned} K'_M &= f_{v1}K_1 + f_{v2}K_2 + f_{vI}K_I \\ E'_M &= f_{v1}E_1 + f_{v2}E_2 + f_{vI}E_I \\ G'_M &= f_{v1}G_1 + f_{v2}G_2 + f_{vI}G_I \\ f_{v1} + f_{v2} + f_{vI} &= 1 \end{aligned} \tag{14}$$

The subscripts *M*, 1 and 2, and *I* denote compound, components 1 and 2, and interphase, respectively. As mentioned in the previous sections, the moisture dependence of elastic moduli is modeled as a function of porosity, which lastly depends on moisture content. In experiments, though, the samples are subject to a certain level of RH, or its other forms such as water activity and chemical potential. The components within a composite may have different moisture contents due to their different hygroscopicity. Therefore, RH rather than moisture content is the more appropriate independent variable. In this study, the moisture content is converted to RH using experimental sorption isotherms (*42*). More details are included in the Supplementary Materials.

The RoM predictions of the elastic properties of M1 are shown in Fig. 3 (D to F). Without interphase, the RoM predictions are generally higher than the measurements. The interphase region, due to the interaction of the two components, is therefore assessed to be weaker than a simple mixture of the two components would be. The RoM predictions of M2 are shown in Fig. 3 (G to I). The findings are similar to those of M1, except that the shear modulus is already well predicted by RoM. It is noted that M1 shows higher scatter than M2 probably due to the smaller system size of M1.

The swelling strain of the matrices can be predicted by the mixture rule, assuming the same swelling strain in mixture as in the components, and the internal stresses taken up by the components according to their volume fractions (*43*)

$$\Delta\varepsilon'_M = \frac{f^0_{v1}E_1\Delta\varepsilon_1 + f^0_{v2}E_2\Delta\varepsilon_2}{f^0_{v1}E_1 + f^0_{v2}E_2} \tag{15}$$

Note that the denominator equals the stiffness of the mixture predicted by RoM. Taking the interphase into account gives

$$\Delta\varepsilon'_M = \frac{f_{v1}E_1\Delta\varepsilon_1 + f_{v2}E_2\Delta\varepsilon_2 + f_{vI}E_I\Delta\varepsilon_I}{f_{v1}E_1 + f_{v2}E_2 + f_{vI}E_I} \tag{16}$$

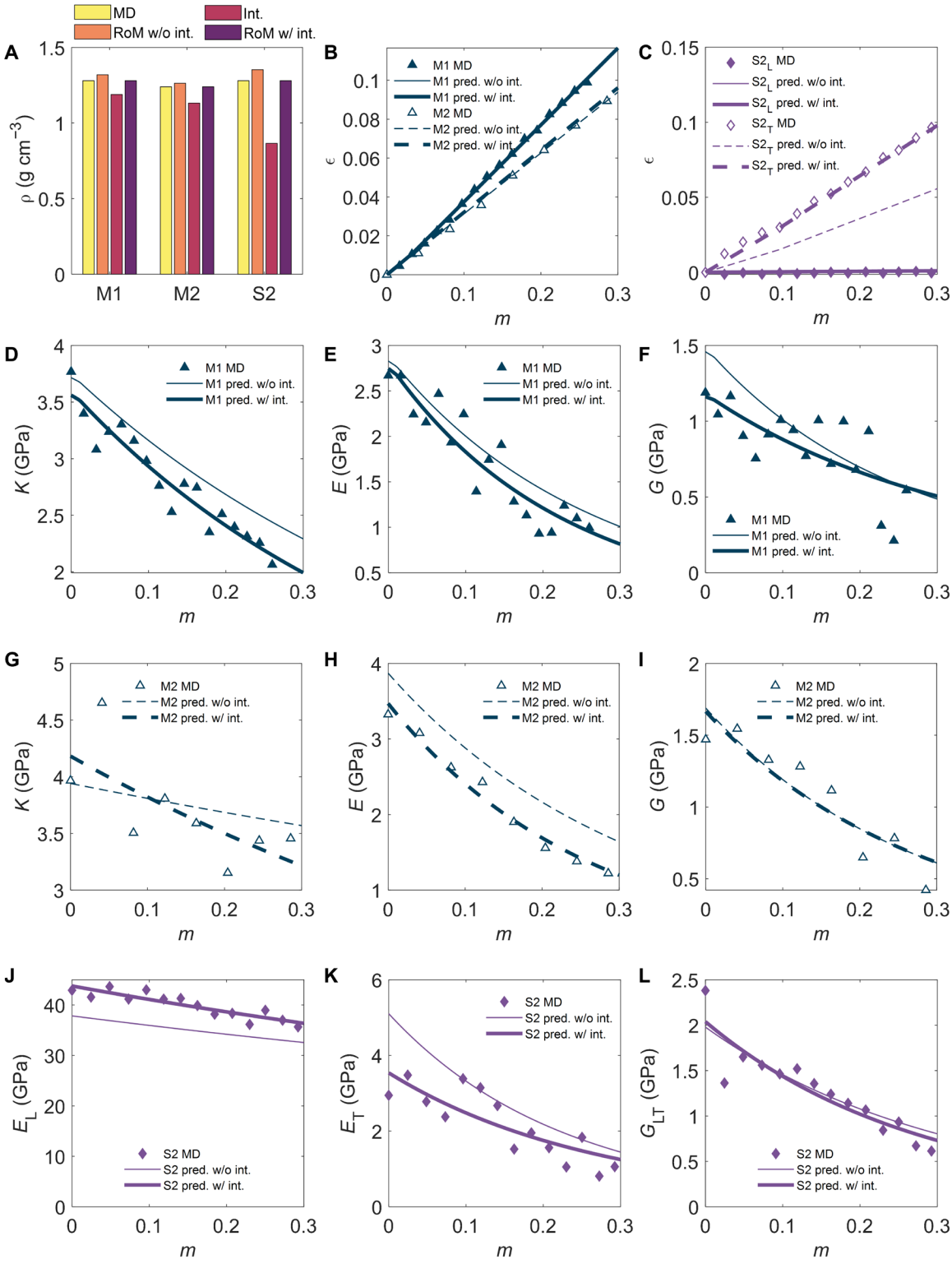

Fig. 3. Mixture rule analyses. (**A**) Density of compounds and interphase predicted by mixture rules. (**B**) Uniaxial swelling strains of M1 and M2, comparison of MD measurements with RoM predictions without (thin lines) and with interphase (bold lines), similarly hereinafter. (**C**) Uniaxial swelling strains of S2 on the longitudinal and transverse directions. Elastic moduli of M1: (**D**) bulk moduli, (**E**) Young's moduli, and (**F**) shear moduli. Elastic moduli of M2: (**G**) bulk moduli, (**H**) Young's moduli, and (**I**) shear moduli. Elastic moduli of S2: (**J**) longitudinal Young's moduli, (**K**) transverse Young's moduli, and (**L**) shear moduli.

Table 3. Density of HBs #HB/V_0 (nm^{-3}) in M1, M2, and S2 at dry condition. $\hat{\delta}$ denotes the fraction of number of HBs formed between the different components.

M1	#HB/V_0 (nm^{-3})	M2	#HB/V_0 (nm^{-3})	S2	#HB/V_0 (nm^{-3})
Total	2.34	Total	5.43	Total	8.50
AGX-uLGN	0.49	GGM-cLGN	0.96	CC-M1	0.02
AGX-AGX	1.14	GGM-GGM	4.15	CC-M2	1.01
uLGN-uLGN	0.72	cLGN-cLGN	0.32	M1-M2	0.30
$\hat{\delta}$	0.210	$\hat{\delta}$	0.176	CC-CC	5.37
				M1-M1	0.37
				M2-M2	1.43
				$\hat{\delta}$	0.156

It is noted that, because the swelling strain depends on the stiffness and the stiffness depends on the porosity and thus swelling strain, Eqs. 13 and 15 and Eqs. 14 and 16 are solved iteratively, respectively.

The swelling strain RoM predictions with and without interphase are shown in Fig. 3B. Unlike in modulus, the interphase does not play an important role in swelling.

Mixture rule analyses of S2 composite

The mixture rules for the S2 composite is in another form because of its transverse isotropy. The CC fibril, denoted by subscript *f*, is moisture independent, exhibiting neither swelling nor weakening. Assuming the fibril to be a transversely isotropic material, the CC phase follows the following elastic relations in the LT plane

$$\begin{aligned}\sigma_{Lf} &= \frac{1}{1-\nu_{LTf}\nu_{TLf}}(E_{Lf}\varepsilon_{Lf}+\nu_{TLf}E_{Lf}\varepsilon_{Tf})\\ \sigma_{Tf} &= \frac{1}{1-\nu_{LTf}\nu_{TLf}}(\nu_{LLf}E_{Tf}\varepsilon_{Lf}+E_{Tf}\varepsilon_{Tf})\\ \tau_{LTf} &= G_{LTf}\gamma_{LTf}\end{aligned} \tag{17}$$

The mechanical properties of CC are moisture independent. The E_L = 90 GPa is measured in MD as described in Materials and Methods. The other values for CC are taken from literature (*44*–*48*): E_T = 42 GPa, G_{LT} = 4.4 GPa, ν_{LT} = 0.38, and ν_{TT} = 0.48.

The elastic behavior of the composite is transversely isotropic, following the same elastic relations as in Eq. 17. The elastic properties of the composite can be derived by applying the following assumptions for the normal stress and strain in longitudinal (Eq. 18) and transverse directions (Eq. 19) and for shear stress and strain (Eq. 20)

$$\varepsilon_L = \varepsilon_{Lf} = \varepsilon_{LM1} = \varepsilon_{LM2}, \sigma_L = f^0_{vf}\sigma_{Lf}+f^0_{vM1}\sigma_{LM1}+f^0_{vM2}\sigma_{LM2} \tag{18}$$

$$\sigma_T = \sigma_{Tf} = \sigma_{TM1} = \sigma_{TM2}, \varepsilon_L = f^0_{vf}\varepsilon_{Tf}+f^0_{vM1}\varepsilon_{TM1}+f^0_{vM2}\varepsilon_{TM2} \tag{19}$$

$$\tau_{LT} = \tau_{LTf} = \tau_{LTM1} = \tau_{LTM2}, \gamma_{LT} = f^0_{vf}\gamma_{LTf}+f^0_{vM1}\gamma_{LTM1}+f^0_{vM2}\gamma_{LTM2} \tag{20}$$

Using these assumptions, the RoMs without interphase for S2 composite can be determined

$$E'_L = f^0_{vf}E_{Lf}+f^0_{vM1}E_{M1}+f^0_{vM2}E_{M2} \tag{21}$$

$$E'_T = 1\Big/\left(\frac{f^0_{vf}}{E_{Tf}}+\frac{f^0_{vM1}}{E_{M1}}+\frac{f^0_{vM2}}{E_{M2}}\right) \tag{22}$$

$$\nu'_{LT} = f^0_{vf}\nu_{LTf}+f^0_{vM1}\nu_{M1}+f^0_{vM2}\nu_{M2} \tag{23}$$

$$G'_{LT} = 1\Big/\left(\frac{f^0_{vf}}{G_{LTf}}+\frac{f^0_{vM1}}{G_{M1}}+\frac{f^0_{vM2}}{G_{M2}}\right) \tag{24}$$

$$\Delta\varepsilon'_L = \frac{f^0_{vM1}E_{M1}\Delta\varepsilon_{M1}+f^0_{vM2}E_{M2}\Delta\varepsilon_{M2}}{f^0_{vf}E_{Lf}+f^0_{vM1}E_{M1}+f^0_{vM2}E_{M2}} \tag{25}$$

$$\Delta\varepsilon'_T = f^0_{vM1}(1+\nu_{M1})\Delta\varepsilon_{M1}+f^0_{vM2}(1+\nu_{M2})\Delta\varepsilon_{M2}-\nu_{LT}\Delta\varepsilon_L \tag{26}$$

The E'_L, E'_T, ν'_{LT}, G'_{LT}, $\Delta\varepsilon'_L$, and $\Delta\varepsilon'_T$ denote the predicted longitudinal modulus, transverse modulus, Poisson's ratio, shear modulus, longitudinal swelling, and transverse swelling, respectively. It is noted that the last term in Eq. 26 takes into account Poisson's effect of the swelling of the composite in the longitudinal direction. Because of the high stiffness of the fiber in the longitudinal direction, the swelling of the composite in this direction, i.e., $\Delta\varepsilon_L$, is very small, and therefore, the last term in Eq. 26 can be neglected.

Similarly, the RoMs with interphase for S2 composite read

$$E'_L = f_{vf}E_{Lf}+f_{vM1}E_{M1}+f_{vM2}E_{M2}+f_{vI}E_I \tag{27}$$

$$E'_T = 1\Big/\left(\frac{f_{vf}}{E_{Tf}}+\frac{f_{vM1}}{E_{M1}}+\frac{f_{vM2}}{E_{M2}}+\frac{f_{vI}}{E_I}\right) \tag{28}$$

$$\nu'_{LT} = f_{vf}\nu_{LTf}+f_{vM1}\nu_{M1}+f_{vM2}\nu_{M2}+f_{vI}\nu_I \tag{29}$$

$$G'_{LT} = 1/\left(\frac{f_{vf}}{G_{LTf}}+\frac{f_{vM1}}{G_{M1}}+\frac{f_{vM2}}{G_{M2}}+\frac{f_{vI}}{G_I}\right) \tag{30}$$

$$\Delta\varepsilon'_L = \frac{f_{vM1}E_{M1}\Delta\varepsilon_{M1}+f_{vM2}E_{M2}\Delta\varepsilon_{M2}+f_{vI}E_I\Delta\varepsilon_I}{f_{vf}E_{Lf}+f_{vM1}E_{M1}+f_{vM2}E_{M2}+f_{vI}E_I} \tag{31}$$

$$\Delta\varepsilon'_T = f_{vM1}(1+\nu_{M1})\Delta\varepsilon_{M1}+f_{vM2}(1+\nu_{M2})\Delta\varepsilon_{M2}+f_{vI}(1+\nu_I)\Delta\varepsilon_I \tag{32}$$

The prediction of Young's moduli is shown in Fig. 3 (J and K). The inclusion of an interphase improves the prediction. The role of interphase is opposite in the two directions. While stiffening the composite in the longitudinal direction, the interphase weakens the composite in the transverse direction. This shows that the interphase is no longer isotropic, but, because of the interaction between matrix and fiber, the interphase becomes transversely isotropic. It is speculated that this anisotropy is due to the alignment of the GGM polymer along the fibril axis due to intensive interaction (*49*). A separate simulation shows that randomly oriented GGM chains will

align with the axial (longitudinal) CC direction when placed next to CC. This behavior is also demonstrated by several experimental studies (*50*–*52*). It is found that the degree of alignment of GGM chains, quantified by the so-called Herman's orientation function (*53*) as shown in fig. S5, is almost not affected by hydration. In general, the formation of interphases weakens the material systems. However, the alignment of GGM chains in S2 induces an interphase that stiffens the longitudinal direction.

The prediction of shear modulus is shown in Fig. 3L. While the RoM with interphase works better in predicting Poisson's ratio, the shear modulus is well predicted by RoMs with or without interphase terms.

The swelling strain RoM predictions with and without interphase are shown in Fig. 3C. In the longitudinal direction, the swelling is almost zero because the cellulose crystal dominates. However, in the transverse direction, the interphase helps the system to swell more. This is in accordance with the mechanical weakening role of the interphase demonstrated above.

In summary, the RoM analyses of this section reveal the formation of an interphase, a region yielded from polymer blending. The interphases are generally weaker than the simple mixture, which is expected because of the immiscibility induced by the hydrophilicity difference between hemicelluloses and LGNs. Under the influence of CC fiber, the soft and isotropic matrix forms a stiff and anisotropic interphase close to the CC fiber. This critical information regarding interphases would be unobtainable without the combination of a comprehensive dataset generated by MD and RoM analyses.

Structure of S2 model and the mechanics of its fiber-matrix interface

This section focuses on the S2 layer model. The structure and working mechanism of S2 will be analyzed in detail and the mechanics of the fiber-matrix interface will be characterized.

Figure 4A is a snapshot of S2 layer model in dry state. The dimensions of the S2 layer model is 10.7 nm by 12.7 nm by 5.3 nm. The density of S2 layer model is 1.28 g cm^{-3}, a value that falls in the range of experimental results (*54*, *55*). The material distribution of the model is shown in Fig. 4 (B and C), where mixture M2 (GGM + cLGN, red and blue) locates next to CC forming an interphase region and mixture M1 (AGX + uLGN, green and orange) forming the bulk matrix. The distribution of GGM is included in the Supplementary Materials.

Enrichment of matrix and water at interface

The spatial density distribution of the matrix and of water is characterized. The density distribution in the matrix under three different moisture contents, i.e., 0.02, 0.16, and 0.3, is shown in Fig. 4 (D to F, respectively), where the three-dimensional (3D) data are projected onto the transverse plane. With increasing moisture content, the dimensions of the system increase, indicating the swelling of matrix material. Meanwhile, the density of matrix decreases with hydration (lighter color), meaning that new pore space is created, especially in the proximity of cellulose fiber surface. The dark spots at the CC interface indicate local density maxima of GGM aligning with the CC. As can be seen from Fig. 4 (G to I), water density increases with moisture content and is evidently higher at the interface and in the interphase region around the fiber. It should be noted that the average interfacial water density is around 0.6 with a peak value of 0.8 g cm^{-3}, lower than that of bulk water (1 g cm^{-3}).

The information can be further reduced into a 1D plot, i.e., density as a function of distance to the CC surface d_{CC}, as shown in Fig. 4J. The density is zero within 0.2 nm of the CC surface, a result of prevailing repulsive forces near the CC surface, a phenomenon usually referred to as depletion. The depletion thickness reflects the interaction of the body with the matrix or water (*56*). For both matrix and water, the density at the interface is higher than in the matrix further away from the CC, showing an enrichment.

The CC plays a vital role in the sorption process of this composite system. While the core of the crystal fiber remains intact, the CC surface is heavily loaded with water molecules. The CC is the load-bearing component of wood cell wall and the CC-matrix interface greatly defines the ability of load transfer, thus the overall mechanical performance of the composite. We therefore study, in more detail, the effect of water enrichment on the interface behavior of the composite, characterized by interface shear strength, hydrogen bonding, etc.

Interface weakening and hydrogen bonding

The interface shear strength is characterized via a pulling test of the CC in the presence of the S2 amorphous polymers. The shear stress displacement curves show stick-slip behavior. In the stick phase, shear stress increases while the displacement remains almost zero. Once the stress reaches a certain limit, called maximum shear stress τ_{max}, the CC abruptly slides for some distance, called slip phase, and then sticks to a new location until the next slip event. The maximum shear stress τ_{max} at different moisture contents is collected and shown in Fig. 4K. Moisture sorption reduces the shear stress by ~3 times, indicating the weakening effect in the interface induced by moisture.

In S2, there are many kinds of HBs formed between the different phases which are matrix-matrix (M-M), CC-CC, water-water (W-W), M-CC, W-M, and W-CC. The number of HBs is normalized by the volume of S2 at dry state (Fig. 4L). The number of HBs can be rescaled to the range of 0 to 1 using Eq. 33 and shown in Fig. 4M

$$\overline{\#\mathrm{HB}} = \frac{\#\mathrm{HB}(m) - \#\mathrm{HB}(0.3)}{\#\mathrm{HB}(0) - \#\mathrm{HB}(0.3)} \tag{33}$$

As can be seen in Fig. 4L, at $m \sim 0$, the CC-CC HBs are the most abundant, accounting for ~65% of the total number of HBs in S2, which agrees well with literature (*57*). The CC-CC HBs stay almost unchanged as sorption goes on, supporting the assertion that CC is not affected by sorption. The adsorbed water stays at the surface instead of entering the crystal core and disrupting the HBs inside CC. It is noted that there is an important number of HBs within the matrix (M-M) and at fibril-matrix interface (M-CC) at dry state.

With sorption, HBs within the matrix and at the fiber-matrix interface are broken, while the number of HBs affiliated with water rapidly grow. In the previous section, we showed that water molecules tend to accumulate at the CC-matrix interface. The water replaces CC-matrix HBs with water-CC (W-CC) and water-matrix (W-M) HBs and thus weakens the interface, causing a reduction of maximum shear stress and its stiffness. The mechanical performance of fiber-reinforced composites depends highly on the stiffness and strength of the fiber-matrix interface. With the weakening of the interface induced by water, it can be expected that the ability of the interface to transfer load will diminish and irreversible deformation can happen.

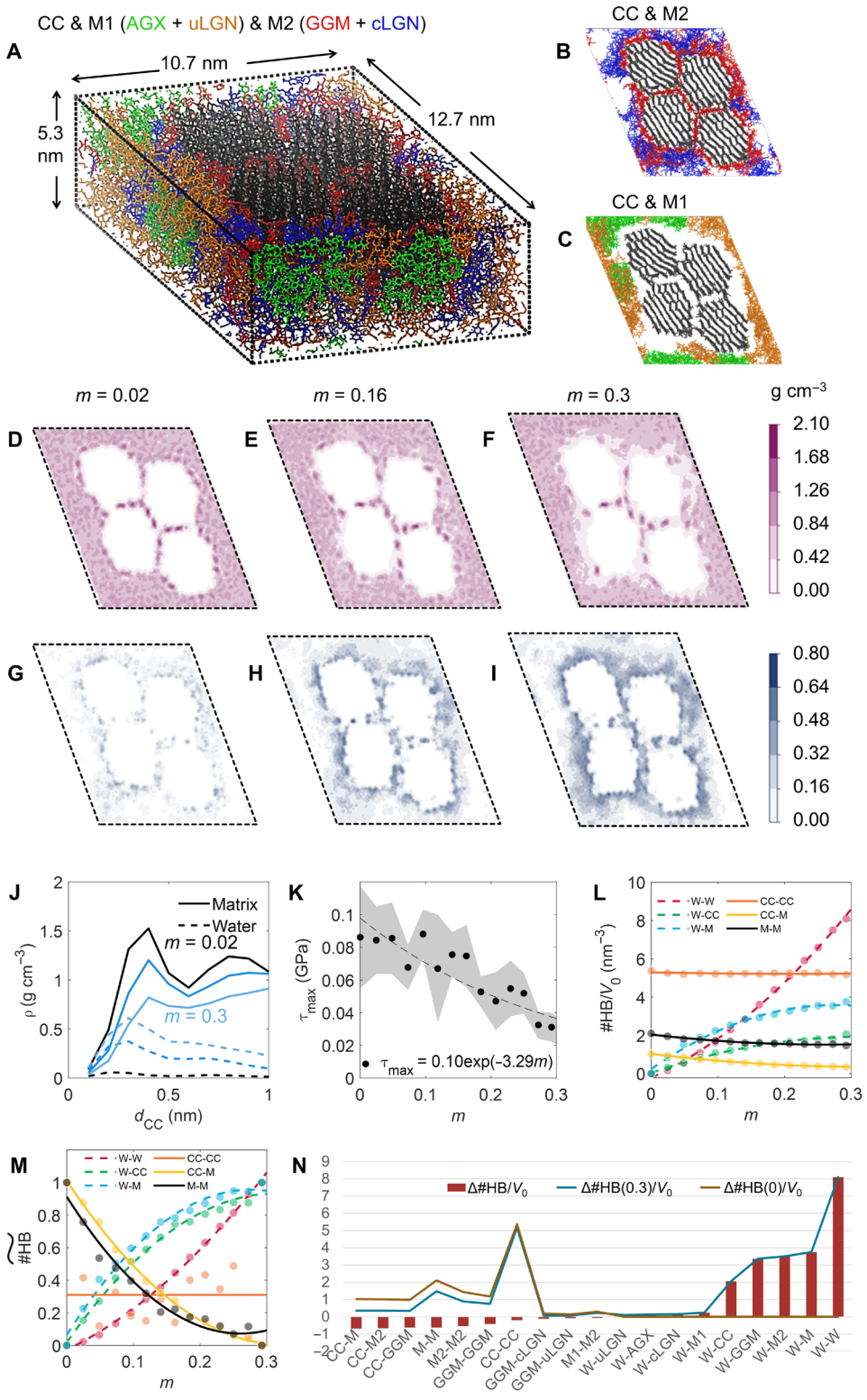

Fig. 4. Structure, distribution of components, interface mechanics, and hydrogen bonding of the softwood cell wall S2 layer atomistic model. (**A**) Three-dimensional view of dry S2 composite. Color denotes different components, namely, CC in black, GGM in red, cLGN in blue, AGX in green, and uLGN in orange. The locations of CC and (**B**) M2 and (**C**) M1. Spatial density distribution of (**D** to **F**) matrix and (**G** to **I**) water at three moisture contents. Note that the CC is white-colored for clarity and is not representing its density. (**J**) Density of matrix and water as a function of distance d_{CC} to the CC surface for three moisture contents, 0.02, 0.16, and 0.3. (**K**) Maximum shear stress as a function of moisture content. (**L**) Absolute number of HBs, and (**M**) rescaled number of HBs within the S2 system in function of moisture content. (**N**) Number of HBs normalized by dry volume: dry condition in green line, $m \sim 0.3$ in blue line, and the difference in brown bars.

The trend of changes in number of HBs can be seen more evidently after rescaling, shown in Fig. 4M. It is noted that the rescaled number of CC-CC HBs seems to fluctuate a lot. However, that is in fact caused by the amplification of the very small amount of total change, i.e., a very small value for the denominator of Eq. 33. The number of matrix-affiliated HBs diminishes and the number of water-affiliated HBs increases. After rescaling, the HBs of CC-M and M-M follow almost the same decreasing curve, while the HBs of W-M and W-CC follow the same increasing curve, showing similar behavior in HB breaking mechanism. This means that matrix and interface show a similar weakening behavior with increasing moisture content.

When the matrix material is categorized into finer subclasses, such as M1 and M2, or even the individual components, such as AGX, uLGN, GGM, and cLGN, many more types of HBs emerge by combination of these categories. While some types remain largely unchanged with hydration and are thus omitted, the most affected types of HBs are shown in Fig. 4N. The x axis is ordered in the

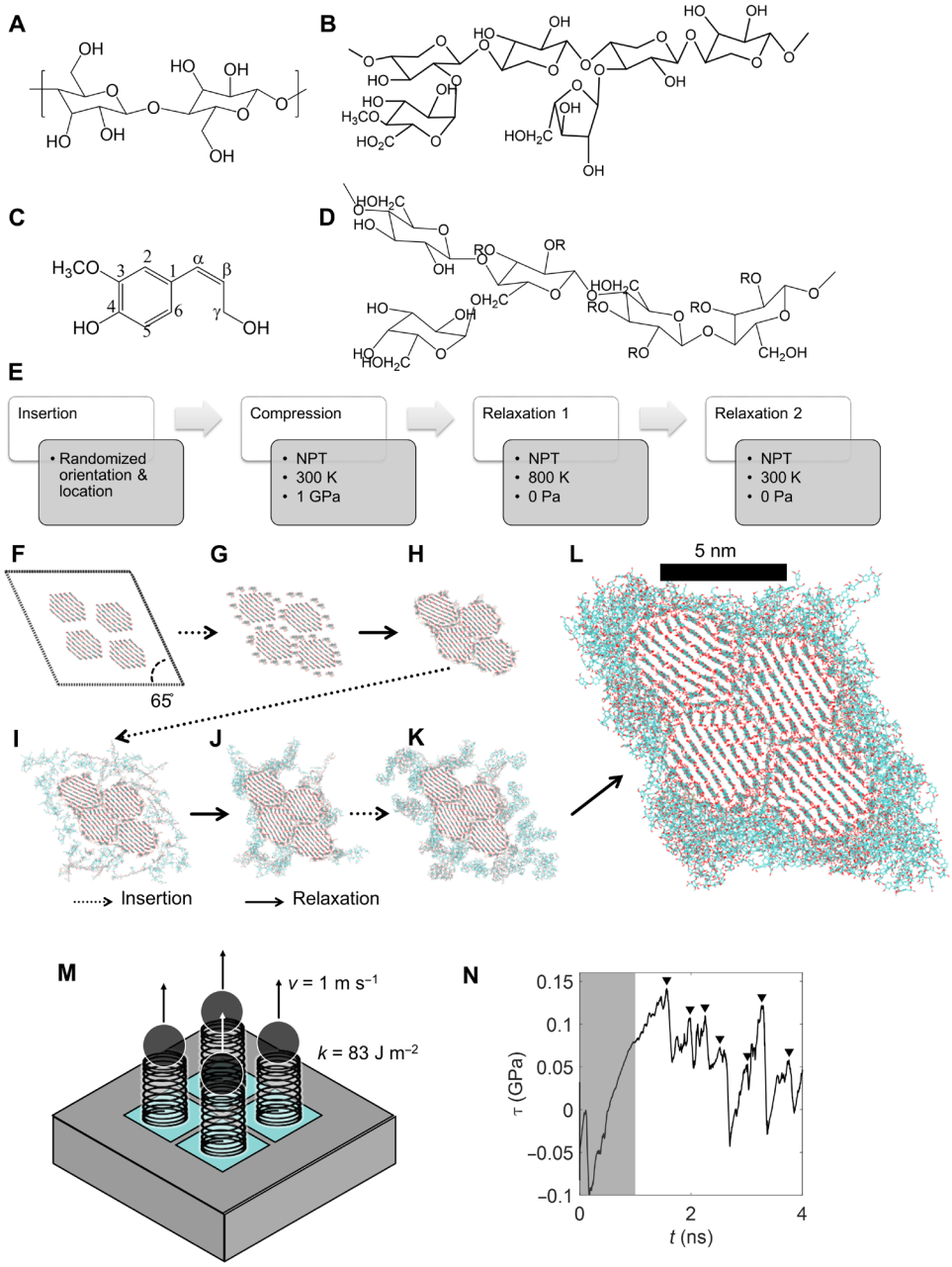

Fig. 5. Preparation of the S2 layer atomistic model and characterization of fiber-matrix interface. The chemical structure of (**A**) CC, (**B**) AGX, (**C**) coniferyl unit for cLGN and uLGN, and (**D**) GGM. (**E**) General procedure for the preparation of a bulk or mixture material system of polymer chains. (**F** to **L**) Assembling procedure of S2 layer model. (**M**) Schematic of pulling test setup. (**N**) Interfacial stress as a function of time of dry S2 system, where the maximum shear stresses associated each with a displacement event are marked with triangles.

ascending of $\Delta\#HB/V_0$. The CC-M HBs suffer the largest loss, and the main reason is the significant loss of CC-GGM HBs. Within the matrix, the largest loss in HBs occurs again for GGM-GGM. This leads to the conclusion that GGM acts as a sort of "glue" between CC and matrix and its moisture dependence plays a fundamental role in the hygromechanical behavior of the composite, especially at the fiber-matrix interface and in the interphase region around the fiber.

DISCUSSION

Multiple pieces of evidence suggest the pivotal role of GGM in cell wall mechanics. For S2 in dry state, the GGM-affiliated HBs are the second most abundant following the HBs formed within CC-CC. The GGM HBs connect CC and the remaining part of the matrix and therefore is essential for the overall mechanical performance of wood cell wall. In the hydrated condition, the GGM-affiliated HBs suffer the most loss in number, especially the CC-GGM HBs. This loss is partly caused by the strong hydrophilicity of GGM and the large number of polar groups at the CC surface next to GGM. Moisture accumulates at the fiber-matrix interface. Such concentration of moisture leads to intensified disruption of interfacial hydrogen bonding, which consequently deteriorates the function of the interface of transferring shear stress. In many applications, wood is used as a load-bearing component. It can be concluded that, to achieve more stable wood material with a reduced tendency of swelling or weakening, the hydrophilicity should be reduced by, e.g., chemical treatment (*58*). It is also possible that, by introducing proper cross-linking between fiber and matrix, the wood mechanical performance is improved (*59*).

Wood is known to be orthotropic. The swelling orthotropy is attributed to multiscale origins, including the alternation of late- and earlywood, the influence of rays, and the arrangements of cells (*23*, *40*). In this study, however, it is shown that the swelling anisotropy originates from the molecular level. The longitudinal swelling of S2 is almost negligible, while the transverse swelling is comparable to the swelling of the matrix materials. The transverse mechanical performance of wood is strongly influenced by hydration. The mixture rule analyses reveal that the mechanics of interphase in S2 is orthotropic, i.e., stiffening and strengthening the composite in the longitudinal direction, while weakening it in transverse directions. It is concluded that the wood cell wall orthotropy stems not only from the oriented CC fiber but also from the presence of an interphase.

It is noted that modeling S2 cell wall is a challenging task with many critical aspects still being revealed by ongoing experimental characterizations. The diameter of microfibrils varies from 3 to up to 60 nm according to various experimental reports (*4*, *5*, *60*, *61*). This study models a microfibril consisting of four cellulose fibrils, which, however, should not be seen as the only possibility. Nonetheless, this study epitomizes the modeling protocol, starting from single components, mixtures, interfaces, and, lastly, reaching composites. Characterizations and validations with available experimental reports are carried out at each level to ensure validity. Other types of plant cell walls, such as bamboo, or even other hierarchical natural materials, such as bone, can be modeled and investigated following a similar framework.

In conclusion, a state-of-the-art atomistic model of softwood S2 layer is constructed using a bottom-up approach, taking great care to reflect the state of knowledge of this cell layer's molecular structure. Individual components of the S2 cell wall layer, including cellulose, glucomannan, xylan, two types of LGN, and two mixtures, are built and mechanically characterized under the full hydration range via separate MD simulations. Hydration is shown to induce fundamental changes to the mechanical and physical properties of all systems. This work provides a complete set of micromechanical properties, including hydrogen bonding, swelling, and weakening, over the full hydration range, which quantitatively agree with available experimental data.

The swelling curves are modeled by a two-section piecewise linear function, reflecting the initial pore-filling regime and the later porosity creation regime. The S2 shows strongly anisotropic swelling, with an almost negligible longitudinal swelling and a transverse swelling comparable to the swelling of the matrix materials. The weakening curves are modeled with power functions of porosity.

The unprecedented micromechanical dataset enables comprehensive RoM analyses revealing the working mechanism of cell wall that is otherwise unobtainable. The interphases of M1, M2, and S2 show densities lower than the bulk that are attributed to either immiscibility or structural mismatch. This hints at possibly weak interactions between the polymer components. Further RoM analyses show that, for M1 and M2, the interphase moduli are smaller than the prediction of simple mixture. The simple mixture is a hypothetical model that assumes zero interaction between the components of a compound. For S2, the situation is a bit more complicated. In the transverse direction, the interphase is weaker than the simple mixture; however, in the longitudinal direction, it is stronger. This

Table 4. Chemical composition of the constructed softwood cell wall S2 layer atomistic model.

Component category	Component polymer	Exp. mass ratio	MD model mass ratio	# Monomers per chain	# Chains
C	CC	27.5% ± 2%*	44.10%	10	36 × 4
	AC	17.6% ± 8%*			
HC	GGM	18.6% ± 9%†	20.90%	10	38 + 20
	AGX	~8%†,‡	7.54%	50	4
LGN	cLGN	~12%*,§	12.08%	2–15	57
	uLGN	~15%*,§	15.39%	50	9

Experimental data: *(*86*). †(*79*). ‡(*87*). §(*88*).

clearly indicates that the orthotropy of the cell wall originates from the cellulose fiber and the interphase. The initially soft and isotropic matrix material becomes stiff and anisotropic under the influence of fiber.

The working mechanism of cell wall is concluded as follows: The cellulose fiber largely defines the modulus and swelling of cell wall, especially along the longitudinal direction. The modulus and structure of the fiber are independent of moisture content. The core of cellulose fiber does not adsorb water. Therefore, it neither weakens nor swells with hydration. In contrast, hemicellulose, the polymer interfacing the LGN and cellulose, is ultrasensitive to moisture. Water tends to severely enrich at the cellulose-hemicellulose interface, deteriorating the HB network and consequently lowering the strength of the fiber-matrix interface characterized by stick-slip stress. Hemicellulose largely determines the mechanics of the fiber-matrix interface and, therefore, the modulus and swelling of cell wall along the transverse direction. The LGN was known to provide recalcitrance and serve as water barriers, etc., although, in the current study, the mechanical role of LGN is seen mainly as interfibril space filler.

This study presents a numerical framework for investigating multicomponent and structurally complex natural biocomposites through molecular simulation. RoM analysis, a simple yet powerful tool, is harnessed to reveal the intricate component interactions in the form of interphase. Not only the obtained cell wall atomistic model opens up direct research opportunities in wood science but also the epitomizing methodology can be extended to other biological hierarchichal systems, such as bone and nacre.

MATERIALS AND METHODS

This section describes the retained material systems, including five components (CC, GGM, AGX, uLGN, and cLGN), two mixtures (M1 and M2), and one composite (S2). Their chemical structures are explained, first reviewing the chemical structures as reported by literature and then presenting the decisions taken toward the atomistic model used for MD simulation, including the different steps in building the systems. Last, the hydration process and mechanical characterization methods are presented.

Preparation of dry polymer systems

General MD parameters

GROMACS 5.0 package (*62*) and GROMOS 53a6 force field (*63*) are used for the MD simulation. GROMOS force field is chosen because it is parameterized on the basis of the free enthalpy of hydration, which is the most important component in the interaction of water with polymer. The integration time step of the equations of motion is 1 fs. The temperature is controlled by the Nose-Hoover thermostat. For isothermal-isobaric ensemble (NPT) simulations, the pressure is controlled by the Parrinello-Rahman barostat. The Coulomb and van der Waals interactions have cutoff radii of 1.0 nm, and the particle-mesh Ewald summation is used to account for long-range Coulomb interactions.

General procedure for preparation of amorphous systems

The chemical structure of CC, coniferyl unit for cLGN and uLGN, GGM, and AGX are included in Fig. 5 (A to D). The procedures to obtain equilibrated molecular structures are the same for GGM, AGX, uLGN, and mixtures 1 and 2, not including cLGN, which is special because of cross-linkages. As summarized in Fig. 5E, generally, the chains are inserted into a very large periodic box with random location and orientation. Then, the box is subjected to a high compression pressure, ~1 GPa, at 300 K. The system is then relaxed at an elevated temperature (800 K) without any pressure applied to allow the release of internal stresses induced by the initial compression. Last, the structures are equilibrated at room temperature at 0 pressure.

Cellulose crystal

The cellulose chemical structure is composed of β(1–4) linked D-glucose units, as shown in Fig. 5A. Although cellulose comprises about half of the mass of cell wall layers and is studied the most among all wood polymers, some basic facts about cellulose are still not clear, such as the number of cellulose chains in a microfibril, the location of amorphous cellulose, and the shape of fiber cross section. Most frequently, researchers assume the number of cellulose chains in a cellulose nanocrystal, the reinforcement phase of the wood cell wall, to be multiples of 6, based on the fact that six cellulose synthase proteins form a cellulose synthase complex subunit (*64*, *65*). Under this premise, researchers propose models composed of 18, 24, and 36 chains based on different indirect measurements (*66*).

In the S2 cell wall layer, it is speculated that cellulose crystals may be in close association with some amorphous cellulose regions on the basis of the observation that rod-like cellulose crystals can be extracted from cellulose fibrils through hydrolysis (*67*, *68*). There are multiple models for the location of amorphous cellulose. It is currently widely acknowledged that the amorphous regions are distributed along the fibril as kinks, formed by strain distortion and twisting during cell formation (*4*, *66*, *69*), However, other reports attribute the existence of kinks to sample processing, as indicated by the non-Gaussian distribution of kink angles of cellulose fibrils (*70*). In this study, amorphous regions of cellulose are not specifically included because of the uncertainty of their presence but also to the need to limit computation costs by controlling the size of the computation domain. Nevertheless, some less perfect CC is present as the cellulose chains at the surface of cellulose nanocrystals are less ordered than the ones at the core.

Hemicelluloses: GGM and AGX

Similar to cellulose, the detailed chemical structures of these hemicelluloses are still under debate, but the retained systems are described below. The validation and characterization of AGX can be found in (*10*). It is reminded that the composition of AGX has three types of monomers, i.e., 67% xylose, 20% glucuronoacid-xylose, and 13% arabinoxylose, which are randomly polymerized. Force field parameters are obtained from the automated topology builder (*71*). For the simulation of pure AGX, the AGX system contains five chains of 100 monomers. When AGX is used in mixture or in S2, a total of four chains of 50 monomers are used for the sake of saving computational costs.

For GGM, two types of monomers, i.e., glucose and mannose, comprise the backbone with a ratio of 1:4, and galactose side groups are branched on mannose (~8 weight %) units. The GGM model is constructed following (*44*). The GGM system consists of four chains of 80 monomers. When GGM is used in mixture, 3 chains of 100 monomers, or in S2, a total of 58 chains of 10 monomers are used. The chain length of GGM in S2 is shortened for the ease of modeling, as shorter chains are easier to disperse randomly in the simulation box of limited size.

The initial structures of these two polymers are built with Material Studio software 8.0 on the basis of the chemical structure indicated above.

LGNs: Condensed and uncondensed types of LGN

LGN has been investigated extensively by experiments, and its chemical structure is known to be tridimensionally complex without a well-defined organization (*72*). Softwood LGN mainly comprises coniferyl units. Depending on the chemical bond types, there are mainly two types of LGN, a more linear type (uncondensed, uLGN) and another more branched type (condensed, cLGN).

For uLGN, the linkages between monomers are all β-O-4, and the polymer chain is linear. The initial structure is built in Material Studio 8.0. The force field parameters for the LGN monomer are built in the automated topology builder (*71*). The polymer chains are assembled into bulk material through the procedure shown in Fig. 5E. Five chains of uLGN with a degree of polymerization of 100 are first placed in a periodic box and equilibrated at 300 K and 0 bar. For the mixture and S2, four chains of 50 monomers are used.

For cLGN, the most common covalent linkage is β-O-4 (40 to 60%), followed by β-5′, 5-5′, β-γ, β-β′, and 4-O-5′ linkages (*51*, *73*). Because of the inherent complexity in cLGN structure, a more sophisticated modeling path, referred to as random branching, must be taken. On the basis of the uLGN structure above, cross-link bonds are added. For force field simplicity, only 5-5′ bonds are considered in this study. When two C5 atoms from two monomers are within 6 Å of each other, a cross-link bond is formed. For 5-5′ bond, an equilibrium bond length of 0.149 nm and bond constant 1.4×10^7 kJ mol^{-1} nm^{-2} are used. Through these steps, a highly bonded system is built. This highly bonded system is used as a template of the initial structure of cLGN. To get the final cLGN, the next step needed is the random removal of some of the linear linkages and/or cross-linkages, thus achieving a randomly branched LGN polymer with the desired ratio of linear to cross-linkages. Then, the structure is energy minimized with steepest descent and conjugate gradient algorithms and equilibrated in NPT ensemble with 300 K and 0 bar. The resulting cLGN is quite heterogeneous and has a distribution of degree of polymerization. In total, the cLGN system consists of 136 cLGN molecules where the number of monomers per molecule ranges from 1 to 43. The Herman's orientation function of the cLGN system shows a value around 0, indicating the isotropy of the built system (*53*). The cLGN in mixture 2 consists of 19 molecules of degree of polymerization (DP) ranging from 1 to 43. The cLGN in S2 consists of 57 molecules of DP ranging from 2 to 15. For all these systems, the ratio of linear to cross-linkages is 2:1 (*51*, *73*).

Because of the complexity of cLGN structure and the ensuing difficulty in modeling and force field construction, cLGN is seldom studied with molecular simulation, especially in the GROMOS force field. It is worthwhile to note that, concurrently with this study, a convenient tool to model the complex 3D structure of LGN in the CHARMM force field was recently developed (*74*), but unfortunately, given the different force field used, this new tool could not benefit this study. Advantages of this method, if applicable here, would have greatly relieved the burden of manually setting up the coordinate and force field files.

Mixtures 1 and 2

The structural arrangement of the cell wall matrix is still subject to debate. Chemical analysis and immunolabeling results reveal that GGM and cLGN are in close proximity to the cellulose fibers, while AGX and uLGN are somewhat further (*75*, *76*). The different components in the cell wall are in a mixture state (*6*), which necessitates the modeling of mixtures of the different types of polymer chains.

Mixture 1 is composed of AGX and uLGN, mass ratio of 1:2. Mixture 2 is composed of GGM and cLGN, mass ratio 7:4. The mass ratios comply with experimental observations of the S2 layer, as summarized in Table 4.

Starting from the chains built in the previous sections, the bulk material is prepared through the procedure shown in Fig. 5E. Different chains are inserted with random locations and orientations to the simulation box and to be then successively compressed and relaxed. Molecules of all types may traverse a boundary and have cross-linkages across the periodic boundaries.

S2 composite

Softwood cell wall S2 layer is composed of cellulose (~45% mass ratio), hemicelluloses (~27%), and LGNs (~28%). There could also be some tiny portion (<3%) of pectins, ions, and extractives that are omitted here because of their reported insignificant roles in mechanics. The mass ratio of different polymers is chemically analyzed and summarized in Table 4.

Softwood S2 layer can be seen as a fiber-reinforced composite where CC is embedded in a multicomponent matrix. The various aforementioned components of S2 need to be positioned in certain arrangements corresponding to the structure of the S2 layer of wood. The exact structural details of each component and their arrangement within the S2 layer are the object of ongoing research, with many critical issues remaining to be clarified (*5*). The state-of-the-art atomistic model of the S2 layer is constructed following the steps described below. As come across situations that required to make assumptions, these are explained.

Four CCs, each consisting of 36 chains of 10-monomer chain forming hexagonal cross sections as shown in Fig. 5F, are first placed in the simulation box separated from each other by at least 1.5 nm. The void spaces are filled in the later assembling steps by the insertion of the other polymers (Fig. 5, G to L). The periodic box is shown with gray lines in Fig. 5F. A nonorthogonal periodic boundary condition is used, where the two base vectors in the transverse plane have an angle of 65°. The depth of the periodic box, i.e., the dimension along the longitudinal direction, is 5.3 nm corresponding to the length of the 10-monomer cellulose chain.

Studies have suggested that hemicellulose is the intermediate polymer joining CC and LGN together (*77*). Quartz crystal microbalance and Fourier transform infrared spectroscopy indicated that CC is closely associated with GGM (*49*). Accordingly, in the MD model, GGM chains are the first to be deposited on the CC surfaces, i.e., 38 chains of GGM inserted next to the surface CC with relatively even distribution (Fig. 5G). From the 38 molecules, 10 are predominantly between two crystals and the rest surrounds the four crystals. It should be noted that the length of the GGM is relatively short, i.e., 10 monomers per chain. As GGM is adjacent to cellulose crystals and enters intercrystal space, forming the so-called microfibril, which is a bundle of CC glued together by GGM, the feasible size of the GGM chain is limited, hence the chosen degree of polymerization of 10. Seven steps of energy minimization and relaxation follow: steepest descent energy minimization, 100-ps relaxation in canonical ensemble (NPT) (300 K) with cellulose fixed, another 100-ps relaxation without constraining cellulose, conjugate gradient energy minimization, 100-ps relaxation in canonical ensemble (NPT) (300 K), 100-ps relaxation in NVT with high temperature (800 K), and 100-ps relaxation in NVT at room temperature and stress-free state. The cellulose atoms are constrained during the high-temperature relaxation to avoid unphysical decrystallization.

Along with GGM, cLGN is also speculated to stay relatively close to cellulose (*6*, *49*), which is supported by the observation that cLGN, similar to GGM, forms an ordered structure aligned to the fiber axis (*50*–*52*). As intermolecular forces are short-range forces, the distance between cLGN and cellulose should be close enough to ensure that the CC can cast an influence over cLGN. Therefore, as the next step of assembling, a mixture of 20 GGM chains and 57 cLGN molecules, mass ratio 3:5, are inserted randomly around the previously built system of cellulose enveloped in GGM (Fig. 5I). Five steps of energy minimization and relaxation are launched: steepest descent energy minimization, conjugate gradient energy minimization, 100-ps relaxation in NVT (300 K), 100-ps relaxation in NVT (800 K), and 100-ps relaxation in NVT (300 K). In addition, in these steps, cellulose atoms are restrained with a strong harmonic potential to prevent the introduction of unphysical defects of the crystal when subjected to high-temperature relaxation. After relaxation, the system reaches the state shown in Fig. 5J. As a point of clarification, mixture 2 studied on its own is a mixture of 58 GGM chains and 57 cLGN molecules, mass ratio 7:4. In the S2 model, the same amount of GGM chains is used, i.e., 58; however, it is noted that 10 of these molecules are mostly located between crystals, slightly changing the amount of GGM in contact with cLGN.

The uLGN and AGX components are then introduced to the system (Fig. 5K), forming the matrix between cellulose microfibrils, as suggested in (*6*). In total, nine chains of uLGN and four chains of AGX, each with 50 monomers per chain, are inserted to the system with a randomly chosen initial location, referred as mixture 1 with ratio 1:2 above. The chains chosen are relatively long here, as an attempt to stay as close as possible to the experimentally reported degree of polymerization (100 to 200) (*78*, *79*). The energy minimization and relaxation steps are as follows: steepest descent and conjugate gradient energy minimization, relaxation in NVT (300 K) for 100 ps, relaxation and densification (3000 bar of pressure on the transverse direction with stress-free on axial direction) in NPT at elevated temperature (400 K) for 1 ns, and another relaxation in NPT (300 K, 0 bar) for 1 ns. In the last step of relaxation, the system gradually recovers from the densified status, and the density is seen to be decreasing and then approaching equilibrium after 0.4 ns. The final state is shown in Fig. 5L. It is noted that Fig. 5L shows only one periodic cell. The S2 model consists of 47,790 atoms and has dimensions of 12.7 nm by 10.7 nm by 5.3 nm.

Hydration

The systems are characterized in dry state and at different moisture contents. In MD, there are various models of water molecule. GROMOS force field is designed to work with either the simple point charge (SPC) or extended simple point charge water models (*80*). The SPC is chosen in this study because its saturation vapor pressure is closer to the value of experiments than the one of SPC/E (*81*).

Regarding obtaining hydrated systems, intuitively, the process of hydration itself could have been modeled with water molecules in a reservoir diffusing into the material. However, such approach would be computationally expensive. Instead, in this study, water molecules are inserted manually one after another, to randomly chosen locations that do not overlap with existing atoms of polymers nor previously inserted water molecules in the system. Following the successful insertion of each water molecule, steepest descent, conjugate gradient energy minimizations, and an equilibration run of 10 ps are carried out. All the polymer systems, except for CC that is not affected by moisture, are subjected to this hydration process. Special care is taken to ensure the hydrated system reaching equilibrium, and the details are included in the Supplementary Materials.

Characterization

HB, swelling strain, elastic moduli, and Poisson's ratio are characterized for the systems including individual polymers, their mixtures, and composite. For the S2 composite model, the density distribution of water and matrix and the interface shear stress are additionally characterized. All systems are tested in the full hydration range seen in wood, i.e., $0 < m < 0.3$, thus reaching what is generally referred to as the fiber saturation point (*82*). In wood, for $m > 0.3$, water inhabits cell lumens, not directly affecting the mechanics of the cell wall.

Hydrogen bond

The establishment of HBs is based on geometric criteria

$$r \leq 0.35 \text{ nm and } \alpha \leq 30° \tag{34}$$

where r is the distance between the donor oxygen atom and the acceptor oxygen atom and α is the angle of acceptor oxygen atom–donor oxygen atom–donor hydrogen atom. The interoxygen distance criterion of 0.35 nm refers to the first minimum of the radial distribution function of SPC water (*83*, *84*). The angle of 30° is approximately the angle of vibrations that break HBs (*85*). All the systems are tested in the moisture content range of 0 to 0.3.

Swelling strain

Swelling strain refers to the uniaxial swelling strain instead of volumetric swelling strain, unless otherwise stated. The uniaxial swelling strain is defined as

$$\epsilon_X(m) = \frac{X(m) - X(0)}{X(0)} \tag{35}$$

where $X(m)$ is the length of the system at moisture content m and $X(0)$ is the size of the system in dry condition using a Lagrangian approach. The uniaxial swelling strains in the three orthogonal directions (ϵ_X, where $X = x, y, z$) of are measured. The volumetric swelling strain ϵ_V is defined similarly except for replacing lateral size X with the volume V. All the systems are tested in the moisture content range of 0 to 0.3.

Elastic constants and Poisson's ratio

For isotropic systems, including GGM, AGX, uLGN, cLGN, mixture 1, and mixture 2, the elastic constants are determined from the slope of the linear regime of stress-strain curves at room temperature. To construct the stress-strain curve for bulk (K), Young's (E), and shear moduli (G), volumetric tensile, uniaxial tensile, and shear strains are applied, respectively, and the resulting stresses are collected. The stresses in MD are computed from the kinetic energy and the virials, as detailed in (*62*). Stepwise strains are applied to a given structure with each step straining around 0.01% of the initial dimension. Every step is followed by a relaxation run of 100 ps to allow molecular rearrangement. The relaxation conditions for bulk, Young's, and shear moduli are different. For bulk moduli, the strained structure is relaxed in the NVT ensemble. For Young's and shear moduli, the structure is relaxed with the strained dimension fixed and the other dimensions coupled to the barostat ($P = 0$ Pa). For example, in Young's modulus measurement, for a sample undergoing uniaxial strain in the x direction, the relaxation will be carried out with the x coordinates fixed, while the y and z coordinates are coupled to a

barostat to allow fluctuation. Because of the stepwise straining and the following relaxation, the influence of the strain rate is minimized. For Young's and shear moduli, the moduli measured in three principal straining directions are collected and averaged. The Poisson's ratio is defined as

$$\nu_{ij} = -\frac{\epsilon_j}{\epsilon_i} \tag{36}$$

with subscripts i and j referring to orthogonal directions.

For the S2 composite, the system is orthotropic because of the CC fiber, where the elastic relation can be expressed as

$$\begin{bmatrix} \epsilon_{xx} \\ \epsilon_{yy} \\ \epsilon_{zz} \\ \gamma_{yz} \\ \gamma_{zx} \\ \gamma_{xy} \end{bmatrix} = \begin{bmatrix} \frac{1}{E_x} & -\frac{\nu_{yx}}{E_y} & -\frac{\nu_{zx}}{E_z} & & & \\ -\frac{\nu_{xy}}{E_x} & \frac{1}{E_y} & -\frac{\nu_{zy}}{E_z} & & & \\ -\frac{\nu_{xz}}{E_x} & -\frac{\nu_{yz}}{E_y} & \frac{1}{E_z} & & & \\ & & & \frac{1}{G_{yz}} & & \\ & & & & \frac{1}{G_{zx}} & \\ & & & & & \frac{1}{G_{xy}} \end{bmatrix} \begin{bmatrix} \sigma_{xx} \\ \sigma_{yy} \\ \sigma_{zz} \\ \tau_{yz} \\ \tau_{zx} \\ \tau_{xy} \end{bmatrix} \tag{37}$$

where ϵ, γ, E, G, ν, σ, and τ denote normal strain, shear strain, Young's modulus, shear modulus, Poisson's ratio, normal stress, and shear stress, respectively.

In the composite, the z axis denotes the longitudinal direction (L). Here, the xy plane is assumed to be isotropic making the composite transversely isotropic, and both x and y axes are denoted as transverse direction (T). In the transverse plane, the following relations are thus established

$$E_x = E_y, \nu_{xz} = \nu_{yz}, \nu_{zx} = \nu_{zy}, G_{TT} = \frac{E_T}{2(1+\nu_{TT})} \tag{38}$$

According to the symmetry of stress and strain tensors, the following relations hold: $\frac{\nu_{zx}}{E_z} = \frac{\nu_{xz}}{E_x} = \frac{\nu_{yz}}{E_y}$, $\nu_{xy} = \nu_{yx}$. To conclude, for S2 composite model, five independent mechanical parameters are needed to describe the constitutive relation: $E_z = E_L$, $E_x = E_y = E_T$, $G_{xz} = G_{zx} = G_{yz} = G_{zy} = G_{TL} = G_{LT}$, $G_{xy} = G_{yx} = G_{TT}$, $\nu_{zx} = \nu_{zy} = \nu_{LT}$.

Spatial density distribution of S2 composite

Spatial density distribution shows the density of matrix or water at a certain location with coordinates (x, y, z). To obtain this distribution, the periodic box is partitioned into a number of cubes of identical volume V_i, volume that equals to the ratio of total volume V of the periodic box to the number of cubes. The center of the cube is (x, y, z). The density of cube i equals the mass of the atoms within that cube divided by the cube volume V_i

$$\rho_i(x,y,z) = \left\langle \frac{\text{mass}(x,y,z,t)}{V_i(x,y,z,t)} \right\rangle_t \tag{39}$$

where the bracket denotes time averaging, over 10 ns of simulation, a time span sufficiently long that spatial fluctuations can be averaged out.

Interface frictional mechanics of S2 composite

To measure the interface frictional mechanics, the CC is pulled along the longitudinal and the stress is extracted. The atoms of CC are attached to a virtual spring of constant $k = 83$ J m^{-2}, which is in the weak spring stiffness case. The other end of the spring is moving at a constant velocity $v = 1$ m s^{-1} along longitudinal axis of CC, as shown in Fig. 5M. The shear stress is defined as the force acting on the virtual spring divided by the surface area of the four CCs, i.e., 353 nm^2. A sample of the stress versus time curve of the dry S2 system is shown in Fig. 5N.

From the curve, the maximum shear stress τ_{max}, shown in Fig. 5N as the peak values marked with triangles, are collected and their averages are reported, as they define the shear strength of the interface. The average value and SD are collected. Pulling tests along two opposite directions ($+z$ and $-z$) are carried out, and the τ_{max} values are averaged. The system is tested in the moisture content range of 0 to 0.3.

SUPPLEMENTARY MATERIALS

Supplementary material for this article is available at https://science.org/doi/10.1126/sciadv.abi8919

View/request a protocol for this paper from *Bio-protocol*.

REFERENCES AND NOTES

1. C. Chen, Y. Kuang, S. Zhu, I. Burgert, T. Keplinger, A. Gong, T. Li, L. Berglund, S. J. Eichhorn, L. Hu, Structure–property–function relationships of natural and engineered wood. *Nat. Rev. Mater.* **5**, 642–666 (2020).
2. D. Fengel, G. Wegener, *Wood* (De Gruyter, 1983).
3. J. Rennel, S. Dillén, K.H.J. Buschow, R. Cahn, M. FLemings, B. Ilschner, E. Kramer, S. Mahajan, P. Veyssière, in *Encyclopedia of Materials: Science and Technology*, K. H. J. Buschow, R. Cahn, M. FLemings, B. Ilschner, E. Kramer, S. Mahajan, P. Veyssière, Eds. (Elsevier, 2001), pp. 7913–7917.
4. A. N. Fernandes, L. H. Thomas, C. M. Altaner, P. Callow, V. T. Forsyth, D. C. Apperley, C. J. Kennedy, M. C. Jarvis, Nanostructure of cellulose microfibrils in spruce wood. *Proc. Natl. Acad. Sci. U.S.A.* **108**, E1195–E1203 (2011).
5. O. M. Terrett, J. J. Lyczakowski, L. Yu, D. Iuga, W. T. Franks, S. P. Brown, R. Dupree, P. Dupree, Molecular architecture of softwood revealed by solid-state NMR. *Nat. Commun.* **10**, 4978 (2019).
6. L. Salmén, I. Burgert, Cell wall features with regard to mechanical performance. A review COST Action E35 2004–2008: Wood machining – micromechanics and fracture. *Holzforschung* **63**, 121–129 (2009).
7. T. Keplinger, F. K. Wittel, M. Rüggeberg, I. Burgert, Wood derived cellulose scaffolds—Processing and mechanics. *Adv. Mater.* **33**, 2001375 (2020).
8. M. Chen, B. Coasne, R. Guyer, D. Derome, J. Carmeliet, Role of hydrogen bonding in hysteresis observed in sorption-induced swelling of soft nanoporous polymers. *Nat. Commun.* **9**, 3507 (2018).
9. K. Kulasinski, R. Guyer, D. Derome, J. Carmeliet, Poroelastic model for adsorption-induced deformation of biopolymers obtained from molecular simulations. *Phys. Rev. E.* **92**, 022605 (2015).
10. C. Zhang, B. Coasne, R. Guyer, D. Derome, J. Carmeliet, Moisture-induced crossover in the thermodynamic and mechanical response of hydrophilic biopolymer. *Cellulose* **27**, 89–99 (2020).
11. A. Rindler, O. Vay, C. Hansmann, U. Müller, Dimensional stability of multi-layered wood-based panels: A review. *Wood Sci. Technol.* **51**, 969–996 (2017).
12. A. Rafsanjani, D. Derome, J. Carmeliet, Poromechanical modeling of moisture induced swelling anisotropy in cellular tissues of softwoods. *RSC Adv.* **5**, 3560–3566 (2015).
13. W. J. Cousins, Elastic modulus of lignin as related to moisture content. *Wood Sci. Technol.* **10**, 9–17 (1976).
14. W. J. Cousins, Young's modulus of hemicellulose as related to moisture content. *Wood Sci. Technol.* **12**, 161–167 (1978).
15. J. Hanus, K. Mazeau, The xyloglucan–cellulose assembly at the atomic scale. *Biopolymers* **82**, 59–73 (2006).
16. S. Besombes, K. Mazeau, The cellulose/lignin assembly assessed by molecular modeling. Part 1: Adsorption of a threo guaiacyl β-O-4 dimer onto a Iβ cellulose whisker. *Plant Physiol. Biochem.* **43**, 299–308 (2005).
17. K. Jin, Z. Qin, M. J. Buehler, Molecular deformation mechanisms of the wood cell wall material. *J. Mech. Behav. Biomed. Mater.* **42**, 198–206 (2015).

18. H. Hao, L. Tam, Y. Lu, D. Lau, An atomistic study on the mechanical behavior of bamboo cell wall constituents. *Compos. Part B Eng.* **151**, 222–231 (2018).
19. S. Youssefian, N. Rahbar, Molecular origin of strength and stiffness in bamboo fibrils. *Sci. Rep.* **5**, 11116 (2015).
20. K. Kulasinski, D. Derome, J. Carmeliet, Impact of hydration on the micromechanical properties of the polymer composite structure of wood investigated with atomistic simulations. *J. Mech. Phys. Solids* **103**, 221–235 (2017).
21. E. Hocker, G. Almkvist, M. Sahlstedt, The Vasa experience with polyethylene glycol: A conservator's perspective. *J. Cult. Herit.* **13**, S175–S182 (2012).
22. K. Murata, M. Masuda, Microscopic observation of transverse swelling of latewood tracheid: Effect of macroscopic/mesoscopic structure. *J. Wood Sci.* **52**, 283–289 (2006).
23. A. Rafsanjani, M. Stiefel, K. Jefimovs, R. Mokso, D. Derome, J. Carmeliet, Hygroscopic swelling and shrinkage of latewood cell wall micropillars reveal ultrastructural anisotropy. *J. R. Soc. Interface* **11**, 20140126–20140126 (2014).
24. M. Chen, B. Coasne, D. Derome, J. Carmeliet, Role of cellulose nanocrystals on hysteretic sorption and deformation of nanocomposites. *Cellulose* **27**, 6945–6960 (2020).
25. K. Kulasinski, L. Salmén, D. Derome, J. Carmeliet, Moisture adsorption of glucomannan and xylan hemicelluloses. *Cellulose* **23**, 1629–1637 (2016).
26. A. Escalante, A. Gonçalves, A. Bodin, A. Stepan, C. Sandström, G. Toriz, P. Gatenholm, Flexible oxygen barrier films from spruce xylan. *Carbohydr. Polym.* **87**, 2381–2387 (2012).
27. A. Höije, M. Gröndahl, K. Tømmeraas, P. Gatenholm, Isolation and characterization of physicochemical and material properties of arabinoxylans from barley husks. *Carbohydr. Polym.* **61**, 266–275 (2005).
28. W. J. Cousins, R. W. Armstrong, W. H. Robinson, Young's modulus of lignin from a continuous indentation test. *J. Mater. Sci.* **10**, 1655–1658 (1975).
29. W. J. Cousins, Elasticity of isolated lignin: Young's modulus by a continuous indentation method. *New Zeal. J. For. Sci.* **7**, 107–112 (1977).
30. L. Muraille, V. Aguié-Béghin, B. Chabbert, M. Molinari, Bioinspired lignocellulosic films to understand the mechanical properties of lignified plant cell walls at nanoscale. *Sci. Rep.* **7**, 44065 (2017).
31. Y. Yu, B. Fei, H. Wang, G. Tian, Longitudinal mechanical properties of cell wall of Masson pine (Pinus massoniana Lamb) as related to moisture content: A nanoindentation study. *Holzforschung.* **65**, 121–126 (2011).
32. W. Gindl, T. Schöberl, The significance of the elastic modulus of wood cell walls obtained from nanoindentation measurements. *Compos. Part A Appl. Sci. Manuf.* **35**, 1345–1349 (2004).
33. X. Wu, R. J. Moon, A. Martini, Tensile strength of Iβ crystalline cellulose predicted by molecular dynamics simulation. *Cellulose* **21**, 2233–2245 (2014).
34. R. Rusli, S. J. Eichhorn, Determination of the stiffness of cellulose nanowhiskers and the fiber-matrix interface in a nanocomposite using Raman spectroscopy. *Appl. Phys. Lett.* **93**, 033111 (2008).
35. A. Šturcová, G. R. Davies, S. J. Eichhorn, Elastic modulus and stress-transfer properties of tunicate cellulose whiskers. *Biomacromolecules* **6**, 1055–1061 (2005).
36. T. Nishino, K. Takano, K. Nakamae, Elastic modulus of the crystalline regions of cellulose polymorphs. *J. Polym. Sci. Part B Polym. Phys.* **33**, 1647–1651 (1995).
37. K. Tashiro, M. Kobayashi, Theoretical evaluation of three-dimensional elastic constants of native and regenerated celluloses: Role of hydrogen bonds. *Polymer* **32**, 1516–1526 (1991).
38. I. Sakurada, Y. Nukushina, T. Ito, Experimental determination of the elastic modulus of crystalline regions in oriented polymers. *J. Polym. Sci.* **57**, 651–660 (1962).
39. L. F. Nielsen, Elasticity and damping of porous materials and impregnated materials. *J. Am. Ceram. Soc.* **67**, 93–98 (1984).
40. F. F. P. Kollmann, W. A. Côte, *Principles of Wood Science and Technology*, E. W. Kuenzi, A. J. Stamm, Eds. (Springer-Verlag, 1968), vol. 2.
41. L. A. Utracki, C. A. Wilkie, *Polymer Blends Handbook* (Springer, 2014).
42. L. Muraille, M. Pernes, A. Habrant, R. Serimaa, M. Molinari, V. Aguié-Béghin, B. Chabbert, V. Aguié-Beghin, B. Chabbert, Impact of lignin on water sorption properties of bioinspired self-assemblies of lignocellulosic polymers. *Eur. Polym. J.* **64**, 21–35 (2015).
43. N. Srisuk, thesis, University of Texas, Arlington, TX (2010).
44. K. Kulasinski, R. Guyer, S. Keten, D. Derome, J. Carmeliet, Impact of moisture adsorption on structure and physical properties of amorphous biopolymers. *Macromolecules* **48**, 2793–2800 (2015).
45. K. Kulasinski, S. Keten, S. V. Churakov, D. Derome, J. Carmeliet, A comparative molecular dynamics study of crystalline, paracrystalline and amorphous states of cellulose. *Cellulose* **21**, 1103–1116 (2014).
46. R. E. Mark, *Cell Wall Mechanics of Tracheids* (Yale Univ. Press, 1967).
47. K. Nakamura, M. Wada, S. Kuga, T. Okano, Poisson's ratio of cellulose Iα and cellulose II. *J. Polym. Sci. Part B Polym. Phys.* **42**, 1206–1211 (2004).
48. L. Chen, A. Li, X. He, L. Han, A multi-scale biomechanical model based on the physiological structure and lignocellulose components of wheat straw. *Carbohydr. Polym.* **133**, 135–143 (2015).
49. L. Salmén, J. Fahlén, Reflections on the ultrastructure of softwood fibers. *Cellul. Chem. Technol.* **40**, 181–185 (2006).
50. R. H. Atalla, U. P. Agarwal, Raman microprobe evidence for lignin orientation in the cell walls of native woody tissue. *Science* **227**, 636–638 (1985).
51. M. Åkerholm, L. Salmén, The oriented structure of lignin and its viscoelastic properties studied by static and dynamic FT-IR spectroscopy. *Holzforschung* **57**, 459–465 (2003).
52. N. Terashima, A new mechanism for formation of a structurally ordered protolignin macromolecule in the cell-wall of tree xylem. *J. Pulp Pap. Sci.* **16**, J150–J155 (1990).
53. P. H. Hermans, P. Platzek, Beiträge zur Kenntnis des Deformationsmechanismus und der Feinstruktur der Hydratzellulose. *Kolloid Zeitschrift* **88**, 68–72 (1939).
54. R. M. Kellogg, F. F. Wangaard, Variation in the cell-wall density of wood. *Wood Fiber Sci.* **1**, 180–204 (2007).
55. M. Zauer, A. Pfriem, A. Wagenführ, Toward improved understanding of the cell-wall density and porosity of wood determined by gas pycnometry. *Wood Sci. Technol.* **47**, 1197–1211 (2013).
56. D. M. Huang, C. Sendner, D. Horinek, R. R. Netz, L. Bocquet, Water slippage versus contact angle: A quasiuniversal relationship. *Phys. Rev. Lett.* **101**, 226101 (2008).
57. A. C. O'Sullivan, Cellulose: The structure slowly unravels. *Cellulose* **4**, 173–207 (1997).
58. P. Samyn, Wetting and hydrophobic modification of cellulose surfaces for paper applications. *J. Mater. Sci.* **48**, 6455–6498 (2013).
59. A. J. Stamm, *Wood and Cellulose Science* (Ronald, 1964).
60. J. J. Lyczakowski, M. Bourdon, O. M. Terrett, Y. Helariutta, R. Wightman, P. Dupree, Structural imaging of native cryo-preserved secondary cell walls reveals the presence of macrofibrils and their formation requires normal cellulose, lignin and xylan biosynthesis. *Front. Plant Sci.* **10**, 1398 (2019).
61. L. Salmén, Micromechanical understanding of the cell-wall structure. *Comptes Rendus Biol.* **327**, 873–880 (2004).
62. M. J. Abraham, T. Murtola, R. Schulz, S. Páll, J. C. Smith, B. Hess, E. Lindah, GROMACS: High performance molecular simulations through multi-level parallelism from laptops to supercomputers. *SoftwareX* **1–2**, 19–25 (2015).
63. C. Oostenbrink, A. Villa, A. E. Mark, W. F. Van Gunsteren, A biomolecular force field based on the free enthalpy of hydration and solvation: The GROMOS force-field parameter sets 53A5 and 53A6. *J. Comput. Chem.* **25**, 1656–1676 (2004).
64. M. Mutwil, S. Debolt, S. Persson, Cellulose synthesis: A complex complex. *Curr. Opin. Plant Biol.* **11**, 252–257 (2008).
65. D. P. Delmer, Cellulose biosynthesis: Exciting times for a difficult field of study. *Annu. Rev. Plant. Physiol. Plant. Mol. Biol.* **50**, 245–276 (1999).
66. S. Y. Ding, S. Zhao, Y. Zeng, Size, shape, and arrangement of native cellulose fibrils in maize cell walls. *Cellulose* **21**, 863–871 (2014).
67. C. Moreau, A. Villares, I. Capron, B. Cathala, Tuning supramolecular interactions of cellulose nanocrystals to design innovative functional materials. *Ind. Crops Prod.* **93**, 96–107 (2016).
68. Z. Liu, X. Li, W. Xie, H. Deng, Extraction, isolation and characterization of nanocrystalline cellulose from industrial kelp (*Laminaria japonica*) waste. *Carbohydr. Polym.* **173**, 353–359 (2017).
69. S. P. Rowland, E. J. Roberts, The nature of accessible surfaces in the microstructure of cotton cellulose. *J. Polym. Sci. Part A 1 Polym. Chem.* **10**, 2447–2461 (1972).
70. I. Usov, G. Nyström, J. Adamcik, S. Handschin, C. Schütz, A. Fall, L. Bergström, R. Mezzenga, Understanding nanocellulose chirality and structure–properties relationship at the single fibril level. *Nat. Commun.* **6**, 7564 (2015).
71. A. K. Malde, L. Zuo, M. Breeze, M. Stroet, D. Poger, P. C. Nair, C. Oostenbrink, A. E. Mark, An automated force field topology builder (ATB) and repository: Version 1.0. *J. Chem. Theory Comput.* **7**, 4026–4037 (2011).
72. G. Gellerstedt, Softwood kraft lignin: Raw material for the future. *Ind. Crops Prod.* **77**, 845–854 (2015).
73. T. Higuchi, in *Biosynthesis and Biodegradation of Wood Components*, T. Higuchi, Ed. (Elsevier, 1985), pp. 141–160.
74. J. V. Vermaas, L. D. Dellon, L. J. Broadbelt, G. T. Beckham, M. F. Crowley, Automated transformation of lignin topologies into atomic structures with ligninbuilder. *ACS Sustain. Chem. Eng.* **7**, 3443–3453 (2019).
75. M. Lawoko, G. Henriksson, G. Gellerstedt, Structural differences between the lignin–carbohydrate complexes present in wood and in chemical pulps. *Biomacromolecules* **6**, 3467–3473 (2005).
76. K. Ruel, J. P. Joseleau, Deposition of hemicelluloses and lignins during secondary wood cell wall assembly. *Hemicellul. Work.* , 103–113 (2005).
77. Y. Takeichi, M. Yoshida, K. Kitano, N. Terashima, H. Yamamoto, In situ measurement of tensile elastic moduli of individual component polymers with a 3D assembly mode in wood cell walls. *J. Wood Sci.* **59**, 104–111 (2013).
78. T. Gorshkova, N. Brutch, B. Chabbert, M. Deyholos, T. Hayashi, S. Lev-Yadun, E. J. Mellerowicz, C. Morvan, G. Neutelings, G. Pilate, Plant fiber formation: State of the art, recent and expected progress, and open questions. *Crit. Rev. Plant Sci.* **31**, 201–228 (2012).
79. R. C. Pettersen, The chemical composition of wood, in *The Chemistry of Solid Wood*, R. Rowell, Ed. (American Chemical Society, 1984), vol. 207 of *Advances in Chemistry*, pp. 57–126.

80. H. J. C. Berendsen, J. R. Grigera, T. P. Straatsma, The missing term in effective pair potentials. *J. Phys. Chem.* **91**, 6269–6271 (1987).
81. J. R. Errington, A. Z. Panagiotopoulos, A fixed point charge model for water optimized to the vapor–liquid coexistence properties. *J. Phys. Chem. B* **102**, 7470–7475 (1998).
82. C. Skaar, *Wood-Water Relations* (Springer Series in Wood Science, Springer Berlin Heidelberg, 1988).
83. A. Luzar, D. Chandler, Structure and hydrogen bond dynamics of water–dimethyl sulfoxide mixtures by computer simulations. *J. Chem. Phys.* **98**, 8160–8173 (1993).
84. A. K. Soper, M. G. Phillips, A new determination of the structure of water at 25°C. *Chem. Phys.* **107**, 47–60 (1986).
85. J. Teixeira, M.-C. Bellissent-Funel, Dynamics of water studied by neutron scattering. *J. Phys. Condens. Matter* **2**, SA105 (1990).
86. J. M. Dinwoodie, *Timber: Its Nature and Behaviour* (Routledge, 2000).
87. H. V. Scheller, P. Ulvskov, Hemicelluloses. *Annu. Rev. Plant Biol.* **61**, 263–289 (2010).
88. D. N.-S. Hon, N. Shiraishi, *Wood and Cellulosic Chemistry*, *Second Edition*, *Revised and Expanded* (Cambridge University Press, 2013), vol. 53.
89. T. C. F. Gomes, M. S. Skaf, Cellulose-Builder: A toolkit for building crystalline structures of cellulose. *J. Comput. Chem.* **33**, 1338–1346 (2012).
90. Y. Nishiyama, P. Langan, H. Chanzy, Crystal structure and hydrogen-bonding system in cellulose Iβ from synchrotron x-ray and neutron fiber diffraction. *J. Am. Chem. Soc.* **124**, 9074–9082 (2002).
91. A. Frey-Wyssling, The fine structure of cellulose microfibrils. *Science* **119**, 80–82 (1954).
92. S. Belbekhouche, J. Bras, G. Siqueira, C. Chappey, L. Lebrun, B. Khelifi, S. Marais, A. Dufresne, Water sorption behavior and gas barrier properties of cellulose whiskers and microfibrils films. *Carbohydr. Polym.* **83**, 1740–1748 (2011).
93. Y. R. J. Eichhorn, The Young's modulus of a microcrystalline cellulose. *Cellulose* **8**, 197–207 (2001).
94. W. Chen, G. C. Lickfield, C. Q. Yang, Molecular modeling of cellulose in amorphous state. Part I: Model building and plastic deformation study. *Polymer* **45**, 1063–1071 (2004).
95. F. R. P. Pienaar, N. J. Eaton, A. Pizzi, Elastic moduli of amorphous cellulose—A conformational analysis approach. *J. Macromol. Sci. Part B* **28**, 115–129 (1989).
96. L. Härdelin, thesis, Chalmers Univsersity of Technology, Gothenburg, Sweden (2018).
97. J. S. Srndovic, thesis, Chalmers University of Technology, Gothenburg, Sweden (2011).
98. K. S. Mikkonen, J. S. Stevanic, K. Pirkkalainen, V. Liljeström, R. Serimaa, L. Salmén, M. Tenkanen, in *ECCM 2012 - Composites at Venice*, *Proceedings of the 15th European Conference on Composite Materials* (2012).
99. W. T. Y. Tze, S. Wang, T. G. Rials, G. M. Pharr, S. S. Kelley, Nanoindentation of wood cell walls: Continuous stiffness and hardness measurements. *Compos. Part A Appl. Sci. Manuf.* **38**, 945–953 (2007).
100. R. Wimmer, B. N. Lucas, Comparing mechanical properties of secondary wall and cell corner middle lamella in spruce wood. *IAWA J.* **18**, 77–88 (1997).
101. W. Gindl, H. S. Gupta, T. Schöberl, H. C. Lichtenegger, P. Fratzl, Mechanical properties of spruce wood cell walls by nanoindentation. *Appl. Phys. A Mater. Sci. Process.* **79**, 2069–2073 (2004).
102. L. Wagner, T. K. Bader, K. de Borst, Nanoindentation of wood cell walls: Effects of sample preparation and indentation protocol. *J. Mater. Sci.* **49**, 94–102 (2014).

Acknowledgments

Funding: This study was supported by the Swiss National Science Foundation grant 162957 (D.D.) and the Office of Naval Research Presidential Early Career Awards for Scientists and Engineers grant N00014163175 (S.K.). **Author contributions:** Conceptualization: C.Z., D.D., and J.C. Methodology: C.Z., S.K., B.C., D.D., and J.C. Formal analysis: C.Z., S.K., B.C., D.D., and J.C. Investigation: C.Z., D.D., and J.C. Data curation: C.Z. Visualization: C.Z. Supervision: D.D. and J.C. Writing—original draft: C.Z. Writing—review and editing: C.Z., M.C., B.C., D.D., and J.C. Funding acquisition: D.D. and J.C. **Competing interests:** The authors declare that they have no competing interests. **Data and materials availability:** All data needed to evaluate the conclusions in the paper are present in the paper and/or the Supplementary Materials.

Submitted 7 April 2021
Accepted 16 July 2021
Published 8 September 2021
10.1126/sciadv.abi8919

Citation: C. Zhang, M. Chen, S. Keten, B. Coasne, D. Derome, J. Carmeliet, Hygromechanical mechanisms of wood cell wall revealed by molecular modeling and mixture rule analysis. *Sci. Adv.* **7**, eabi8919 (2021).

ScienceAdvances

Hygromechanical mechanisms of wood cell wall revealed by molecular modeling and mixture rule analysis

Chi ZhangMingyang ChenSinan KetenBenoit CoasneDominique DeromeJan Carmeliet

Sci. Adv., 7 (37), eabi8919. • DOI: 10.1126/sciadv.abi8919